Comparative Study of Mg and Mg-RE Alloys for Battery Applications

A Thesis
Presented in Partial Fulfillment of the Requirements for the
Degree of Master of Science
with a
Major in Materials Science and Engineering
in the
College of Graduate Studies
University of Idaho
by
Nikunja Shrestha

Major Professor: Dr. Krishnan Raja, Ph.D.
Committee Members: Dr. Vivek Utgikar, PhD.; Dr. Indrajit Charit, PhD.;
Dr. I. Francis Cheng, Ph.D.
Department Administrator: Dr. Eric Aston, Ph.D.

May 2019

Authorization to submit thesis

This thesis of Nikunja Shrestha submitted for the degree of Master of Science in Materials Science and Engineering titled "Comparative Study of Mg and Mg-RE alloys for Battery Applications" has been reviewed in final form. Permission, as indicated by the signatures and dates below, is now granted to submit final copies to the College of Graduate Studies for approval.

Major Professor: …………………………… Date:……………………

Dr. Krishnan S. Raja, Ph.D.

Committee Members: …………………………… Date:……………………

Dr. Indrajit Charit, Ph.D.

…………………………… Date:…………………

Dr. Vivek Utgikar, Ph.D.

……………………………. Date:…………………..

Dr. I F. Cheng, Ph.D.

Department
Administrator: ……………………………. Date:…………………...

Dr. Eric Aston, Ph.D.

Abstract

Mg-air batteries are considered important power sources especially for vehicles because of their remarkable high theoretical energy density and low cost. Mg-air batteries have a theoretical energy density of 6800Wh/kg, specific capacity of 2200 Ah/kg, and a theoretical cell voltage of 3.1V. The theoretical performance of Mg-air battery shows its comparability with Li-ion battery and can also considered better due to its low toxicity and easy availability. But, Mg-air battery has some limiting factors like low operating voltage, low columbic efficiency due to parasitic reactions such as hydrogen evolution, sluggish oxygen reduction reaction kinetics at air cathode. Our project will focus on the corrosion mechanism of magnesium and Mg-RE alloys in different electrolytes with particular reference to HER and battery discharge. The polarization behavior of different Mg- Rare earth alloys were evaluated in different heat-treated conditions and different surface conditions along with volumetric determination of hydrogen gas evolved during cathodic and anodic polarization.

Mg-RE alloy ZE10A in three different heat treatment condition (a) as received, (b) heat treatment at 525^{o} C for 8 hours and (c) 525^{o}C for 24 hours was evaluated to observe the relationship between corrosion rate and grain size of the Mg sample. Similarly, commercial purity Mg, Mg-RE alloys ZE10Aand EV31A were evaluated in as received condition for potential application as anode for Mg-air battery. Anodic and cathodic polarization studies were performed in 0.6M NaCl, 0.5M $NaNO_3$ and 0.1 M Na_2SO_4 electrolytes. Hydrogen evolved during anodic polarization was measured at different potentials and electrochemical impedance spectroscopy was carried out at open circuit conditions. The discharge behavior of lab made battery was also tested to compare the performance of the alloys in the battery.

There is no unequivocal relation is available to describe the effect of grain size on the corrosion behavior. Several reports point out improvements in the corrosion resistance of the Mg alloys upon grain refinement. A decrease in the corrosion resistance has also been observed with the decrease in the grain size for different materials such as pure Mg, Al alloy, and Ni-base alloy. Ralston et al. correlated the improvement in the corrosion resistance by the grain refinement to the ability of the metal to form a protective passive layer by improved ionic conduction of the grain boundaries. The refinement of grain is generally achieved by severe

plastic deformation processes such as such as surface mechanical attrition, equal channel angular pressing (ECAP), and friction stir processing. Reduction in grain size is also associated with other microstructural changes such as increased dislocation density, point defects, and creation of internal stresses during these mechanical processing techniques. Therefore, the observed changes in the corrosion behavior due to variations in the grain size cannot solely be attributed to the grain boundary structures. In order to isolate the effect of grain size, other parameters such as dislocation density, defect structures, phase content, secondary phases and their composition, shape, size, and volume fraction need to be maintained at the same level and only the grain size should vary. In this work, the effect of grain size on the corrosion of ZE10A has been investigated without subjecting the material to plastic deformation.

Magnesium exhibits a phenomenon known as negative differential effect which is characterized by the increase in the rate of hydrogen evolution with increasing anodic potential. The strategy for minimizing the NDE effect would be to decrease the impurity elements to very low levels and add elements such as arsenic that will poison the hydrogen recombination and minimize the hydrogen evolution. Another strategy to minimize hydrogen evolution is to design new electrolytes. In a recent study, Richey et al showed that hydrogen evolution was the highest in 0.5 M NaCl solution and the lowest in 0.5 M $NaNO_3$ solution. In the research, anodically polarized Mg surface was found to comprise of $Mg(OH)_2$/MgO based bilayer film which presented a peculiar problem, as ideally a hydroxide film would slow down the kinetics of the electrochemical reaction, but it seemed to enhance the kinetics of hydrogen evolution reaction. Mg surface was found to be proportional to the rate of film growth. Many studies have shown that Mg undergoes rapid dissolution accompanied by $Mg(OH)_2$ layer forming spontaneously upon the surface which could enhance parasitic corrosion in primary Mg batteries and affect the efficiency of Mg and decrease the life span of Mg alloys used in light weight applications. The volumetric HE collection method is used for calculation of corrosion rate during anodic polarization. The volume of the hydrogen collected is used to calculate the reduced Columbic efficiency of the battery based on the relation:

$$Q\ \text{total} = Q_{H2} + Q_{i\ \text{net anodic}}.$$

The main aim of the work is to investigate the polarization behavior Mg-rare earth (RE) alloys such as ZE10A (Elektron 717) and EV31A (Elektron 21) as potential anodes for Mg-air battery, and compare their behavior with that of commercial purity Mg. The rationale behind selecting these alloys is to understand the role of Zn and Nd alloying additions on the anodic activation of the magnesium surface for battery application. Furthermore, electrochemical characterization was carried out in three different electrolytes consisting of NaCl, Na_2SO_4 and $NaNO_3$ salts to understand the role of electrolyte on the NDE of the Mg-RE alloys.

Acknowledgements

I would sincerely like to thank my major Professor Dr. Krishnan S. Raja for giving me with this opportunity to work under his guidance. I am very grateful for his trust, time, patience and encouragement throughout my program. My project would not been completed without his guidance. I would also like to thank Dr. Vivek Utgikar, Dr. Indrajit Charit and Dr. I.F. Cheng for their support throughout the duration of project. I am also grateful to Dr. Thomas Williams for helping me with the instrumental analysis part of project.

Dedication

This thesis is dedicated to my family, my wife, my friends and all my professors who directly and indirectly played important role in helping me finish my thesis.

Table of Contents

List of Figures

List of Tables

Chapter 1: Introduction

1.1 Motivation

The growing concern about energy crisis and pollution has led to the need of renewable clean energy storage rechargeable batteries. So, different energy sources like lead-acid, Ni-Cr, nickel-metal hydride, lithium-ion, fuel cells and metal air batteries are explored and developed [1]. Among these, metal air batteries have received great interest due to a huge theoretical energy density of 2 to 10 folds higher than lithium ion batteries and low cost. The metal air batteries involve the electrochemical coupling of a reactive metal anode to an air cathode. The reactive metal anode is oxidized electrochemically by air. The metal air batteries are believed to be primarily used for applications in electric vehicles due to their high density, recharge ability and ambient temperature operation. Different reactive metals can be used in metal air batteries as anode. The table below shows the characteristics of metal air cells [2].

Table 1.1: Characteristics of Metal-Air Batteries

Metal Anode	**Electrochemical Equivalent (Ah/gm)**	**Theoretical Cell Potential (V)**	**Theoretical Specific Energy (Wh/g)**	**Practical Operating Potential (V)**
Li	3.86	3.4	13	2.4
Ca	1.34	3.4	4.6	2.0
Mg	2.20	3.1	6.8	1.4
Al	2.98	2.7	8.1	1.6
Zn	0.82	1.6	1.3	1.2
Fe	0.96	1.3	1.2	1.0

As seen from the table, Li has the highest theoretical specific energy of 13.0 kWh/kg which is significantly greater than other rechargeable battery technologies but Li air batteries still have disadvantages like instability of lithium in humid environments, low electrochemical efficiency owning to high charging over potentials, poisonous bi-products. The use of non –

aqueous electrolytes in Li air batteries raises cost and safety issues. The decomThe decomposition of lithium peroxide in this battery makes it poisonous and explosive. Even though it demonstrates improved charge transport, lithium is costly compared to other elements like aluminum and magnesium. The Zn-air batteries also suffer from different problems like zinc precipitation, zinc anode, dendrite formation, non-uniform zinc dissolution, limited oxygen solubility in electrolytes and higher charge potentials [4]. This has given rise to the popularity of magnesium and aluminum batteries. But still the batteries have problems like high self-discharge rate, sluggish discharge kinetics, lack of recharge ability and short shelf life. In case of both magnesium and aluminum, a passive layer is formed which stops the further reaction to occur. Thus the breakdown of passive film is important in order for the anode to be operated as a reversible electrode in aqueous solution. The standard Gibbs free energy of $Mg(OH)_2$ is -833.7kJmol^{-1} compared to -1582.3kJmol^{-1} of Al_2O_3 and -1306.0 kJmol^{-1} $Al(OH)_3$ established a very high barrier leading to the possibility of poor interfacial kinetics of further dissolution of aluminum anode[5]. So, this project mainly focuses on the analysis of different magnesium alloys and select it as an anode for Mg-air battery.

1.2. Objectives

- To investigate Mg-RE alloys as potential Anode materials
- Use of Arsenic oxide as additive to control the hydrogen evolution reaction

References

1. American Society for Metals. (1986). *Metals Handbook Desk Edition. Metals.* Park, OH: American Society for Metals.
2. Rand, D.E., (1979).*Battery Systems for Electric Vehivels:State of Art Review.* J.Power Sources,101
3. Liu, Y., Sun, Q., Li, W. Adair, K.R., Li, J., & Sun, X. (2017) *A Comprehensive Review on Recent Progress in Aluminum-Air Batteries.* Green Energy & Environment, 246-277
4. Lee J.S., Kim S.T., Cao R., Choi N.S., Liu M., Lee K.T.,& Cho J. *Metal-Air Batteries with High Energy Density:LI-Air versus Zn-Air.* Advanced Energy Materials.
5. American Society for Metals. (1986). *Metals Handbook Desk Edition. Metals.* Park, OH: American Society for Metals.

Chapter 2: Literature Review

2.1. History of Metal Air Batteries

Research on metal air batteries started before lithium ion batteries. The first primary zinc air battery was designed by Maiche in 1878 and its commercial products started to enter the market in 1932[6]. After that, aqueous iron –air, aluminum-air and magnesium-air batteries were developed in 1960s [7]. Despite the early beginning the development of metal air batteries, they usually suffer from problem with metal anodes, air catalysts and electrolytes which makes it hard for large scale production and replacing Li-ion batteries for future applications. Anode polarization instability, parasitic corrosion and non-uniform dissolution has prevented their further development.

Metal air batteries still faces the challenges like the reaction of anode with electrolyte to form a passivation layer. The film causes an irreversible loss in battery performance. The other reason is the probability of growth of dendrite on anodes which is the result of uncontrollable dissolution and deposition of metal anodes. It is also very difficult to find the electrolyte with all the desired properties which include high stability, low volatility, non-toxic and high oxygen solubility and development of an efficient cathode. Many researches are being conducted on the metal air battery to make the battery more efficient [8].

2.2 Working of Metal Air Batteries

The metal air batteries usually use neutral or alkaline electrolytes. The use of acidic electrolytes cause the metals to be used up very fast causing the battery life to be very short where as highly alkaline solution causes the formation of oxide layer on the metal resulting in the stoppage of anodic reaction with the solution. Thus, neutral or slightly alkaline electrolytes are comparatively better choice for the efficient operation for longer duration of time. During discharge, metal is oxidized at the anode; oxygen from the surrounding air is reduced on the catalyst particles supported at the gas diffusion cathode and is given by the following equations [11]:

$$\text{Anode: } M \longrightarrow M^{n+} + ne^-$$

$$\text{Cathode: } O_2 + ne^- + 2H_2O \longrightarrow 4OH^-$$

where, M presents the metal and n is the oxidation number of the metal ion. In neutral solution, the oxygen is reduced to OH^- at the interface of the gas solid liquid ternary phases in the air cathode. The possible reaction pathways involved in the ORR in a neutral solution can be expressed as [12]:

$$O_2 + 2H_2O + 4e^- \longrightarrow 4OH^-$$

$$O_2 + H_2O + 2e^- \longrightarrow HO_2^- + OH^-$$

$$HO_2^- + H_2O + 2e^- \longrightarrow 3OH^-$$

$$2HO_2 \longrightarrow 2OH^- + O_2$$

But the sluggish kinetics of the oxygen reduction reaction causes the large over potential and high polarization which lead to the bad performance of the battery.

2.3 Types of Metal Air Batteries

2.3.1 Lithium air batteries

Li air battery is comparatively most efficient because of its highest theoretical voltage and electrochemical equivalence of ($3860 Ah.Kg^{-1}$). The cell discharge reaction for Li-air battery is given below:

$$2Li + H_2O + 1/2O_2 \longrightarrow 2LiOH \qquad E^o = 3.35V$$

Lithium metal, atmospheric oxygen and water are used during discharge and excess LiOH is produced. The cell can also operate at high columbic efficiencies because of the formation of protective film which prevents the rapid corrosion. The self-discharge of lithium metal is very fast due to parasitic corrosion reaction at low open circuit and drain discharge.

$$Li+H_2O \longrightarrow LiOH+1/2H_2$$

The above reaction degrades the anodic columbic efficiency and must be controlled in order to achieve the full potential of lithium-air batteries. The major advantage of Li-Air batteries is its high cell voltage but this type of battery has issues with availability, cost and safety so, researches are being done on other materials rather than lithium to address these problems [10].

Li-air batteries can be divided into four types depending on the nature of electrolyte. They can be non-aqueous, aqueous, hybrid and all solid-state electrolyte. All these four systems use Li metal as anode and oxygen gas as cathode. But the reaction mechanism differs according to the electrolyte [14].

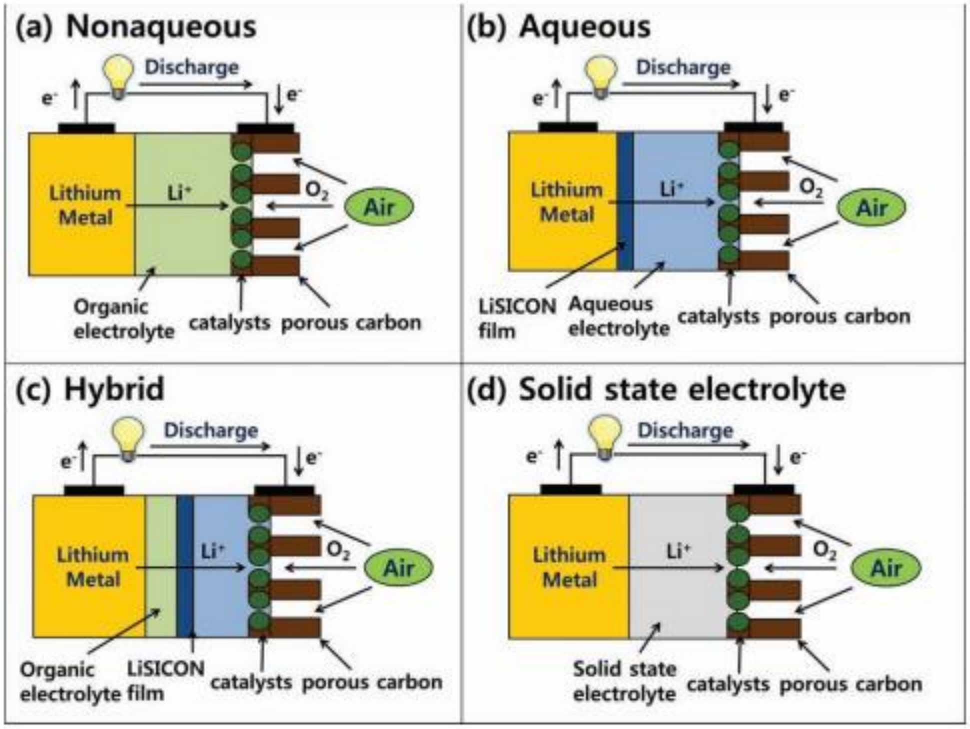

Figure 2.1: Types of Li-Air Batteries

The configuration of non-aqueous electrolyte system is similar to that of conventional Li-ion batteries. Conventional Li-ion batteries use carbon or alloy materials as anodes, Li metal oxides or phosphates as cathodes, and Li salt dissolved in aprotic solvents as electrolytes. Li-air batteries use oxygen gas as a cathode material and porous carbon and catalyst composites must be added as the Li_2O_2 reservoir in the cathode. The major difference between the two systems is that an open system is required for Li-air batteries because the oxygen is obtained from the air [15-17].

The non-aqueous electrolyte follows the following stepwise reaction mechanism:

$$2Li+O_2 \longrightarrow Li_2O_2 \qquad E^o=3.10V \text{ vs } Li/Li^+$$

$$4Li+O_2 \longrightarrow 2Li_2O \qquad E^o=2.91V \text{ vs } Li/Li^+$$

Standard cell potential, E^o were calculated using the standard Gibbs free energy of formation. But recently, Lu et al. revised this theoretical reversible potential of above equations to come up with the following equations [18]:

$$2Li+O_2 \longrightarrow Li_2O_2 \qquad E^o=2.96V \text{ vs } Li/Li^+$$

$$4Li+O_2 \longrightarrow 2Li_2O \qquad E^o=2.91V \text{ vs } Li/Li^+$$

Laoire et al. carried out a fundamental study of the influence of solvents on the oxygen reduction reaction (ORR) to elucidate the reaction mechanism of the oxygen electrode and based on the electrochemical analysis and XRD experiments, they suggested the following O_2 reduction processes [19,20].

$$Li^++e-+O_2 \longrightarrow LiO_2 \qquad E^o=3.0 \text{ V vs } Li/Li^+$$

$$2LiO_2 \longrightarrow Li_2O+O_2 \qquad \text{Chemical reaction}$$

$$Li^++e^-+LiO_2 \longrightarrow Li_2O_2 \qquad E^o=2.96V \text{ vs } Li/Li^+$$

$$2Li^++e^-+Li_2O_2 \longrightarrow 2Li_2O \qquad E^o=2.91V \text{ vs } Li/Li^+$$

The first product is lithium superoxide involving one electron process. These reactions are kinetically irreversible or quasi-reversible electrochemical processes, resulting in high polarization for the oxygen evolution reaction.

The hybrid version was introduced by Zhou group who used the hybrid electrolyte, 1M $LiCLO_4$ in ethylene carbonate dimethyl carbonate and 1M KOH aqueous solution separated by a LISICON ($Li_{1+x+y}Al_xTi_{2-x}Si_yP_{3-y}O_{12}$) film. Various ionic conducting glass-ceramic protective double layers have been introduced to improve the charge transfer reaction of Li ions between Li metal and aqueous electrolytes [21, 22].The solid state Li-air battery was demonstrated by Kumar et l. The cell is composed of a Li metal anode an Li-ion conductive solid electrolyte membrane laminate fabricated from glass-ceramic and polymer-ceramic powder. The sample exhibited good thermal stability and recharge ability in the range of 30 to 105ºC [23].

All the above systems are considered to be promising and much attention has been attracted by all species of Li-air batteries. However, many problems still need to be solved and practical issues need to be addressed.

2.3.2 Zinc air batteries:

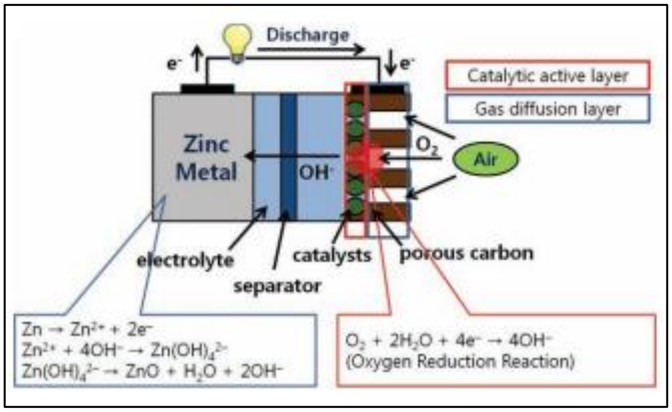

Figure2.2: Schematic of Zinc-Air Battery [14]

Zinc batteries are one of the promising candidates for building an efficient Metal-Air batteries. Zinc is comparatively more available, less toxic and cheaper in cost than Li-Air battery [24-26]. Zinc air batteries are easier to manufacture and are made from more common and less costly materials. Zinc air battery hold a very large potential to replace Li-ion batteries in electric vehicle. But their low power density and limited cycle life is still limiting them to be used in electric vehicle. The anode of the zinc air battery suffers from dendrite formation, shape change and passivation which leads to poor life cycle [27].

Even though zinc air batteries are not as energy dense as lithium air or aluminum air batteries, they are electrically rechargeable to limited number of cycles and do not suffer from any outside reactions as lithium air batteries [28].The lithium air battery also faces challenges like moisture sensitivity, poor rate capability and irreversible side reactions resulting in low cycles life, safety hazards and low power density [29].Due to these challenges, many researchers are being attracted to Aluminum air batteries but aluminum batteries are not rechargeable so Zinc air batteries also have gained lot of attention [30]. Zinc anode exhibits electrode potential of 1.26V vs SHE and possess a theoretical specific capacity of 819mAh/g [31].

Zinc air batteries are composed of three parts zinc metal as an anode, air electrode as the cathode which is divided into a gas diffusion layer and a catalytic active layer and a separator. Oxygen from atmosphere diffuses into the porous carbon electrode by the difference in pressure of oxygen between the outside and inside of the cell and catalyst facilitates the reduction of oxygen to hydroxyl ions in the alkaline electrolyte with electrons generated from the oxidation of zinc metal as the anode reaction.[10]

The overall cell reaction of a zinc air battery on discharge in an alkaline electrolyte is

$$Zn+1/2O_2+H_2O+2(OH) \longrightarrow Zn\ (OH)_4^{-2} \qquad E^o=1.62V$$

The initial discharge reaction at the zinc electrode can be simplified to

$$Zn+4OH^{-}Zn\ (OH)_4^{-2}+2e$$

The reaction occurs as a result of the solubility of the zincate anion in the electrolyte and proceeds until the zincate level reaches the saturation point. There is no well-defined solubility limit, since the degree of super saturation is time dependent. After partial discharge the solubility exceeds the equilibrium solubility level with subsequent precipitation of zinc oxide as follows:

$$Zn\ (OH)_4^{-2} \longrightarrow ZnO+H_2O+2(OH)^-$$

The overall cell reaction then becomes:

$$Zn+1/2O_2 \longrightarrow ZnO$$

The transient solubility is one of the main reasons for the difficulty in making a successful rechargeable zinc/air battery. The location of the precipitation of the reaction product cannot be controlled so that on a subsequent recharge the amount of zinc deposited on different parts of the electrode area of the cell can vary [10].

Different types of zinc air batteries are portable zinc air batteries is an effective way to package the zinc air system in small sizes. The anode/electrolyte blend is similar to the anode blend used in zinc alkaline primary cells containing zinc powder in a gelled aqueous potassium hydroxide electrolyte. The cathode is a thin gas diffusion electrode comprising two layers, an active layer and a barrier layer. The active layer of the cathode which interfaces with the electrolyte, uses a high surface area carbon and a metal oxide catalyst bonded together with Teflon. The high surface area carbon is required for oxygen reduction and the metal oxide catalyst (MnO_2) for peroxide decomposition [32]. The other type is Industrial Primary Zinc/ Air batteries which have been used for many years to provide the low rate, long life power for application such as railroad signaling and remote communications. One type of these batteries are preactivated and water activated type of batteries. A typical preactivated industrial type of zinc air batteries has a bed of lime to absorb carbon dioxide and to remove soluble zinc compounds from solution and precipitate them as calcium zincate. The cell is activated by adding appropriate amount of water to dissolve the potassium hydroxide. In the other type of cell, gelled electrolyte to eliminate the possibility of leakage during operation is used and the zinc electrode is composed of zinc powder mixed with a gelling agent and the electrolyte. The reaction product is zinc oxide rather than calcium zincate [33]. The other type of zinc air batteries is the hybrid air or manganese dioxide batteries in which a hybrid cathode containing a significant amount of manganese dioxide is used. During the low rate operation the battery functions as a zinc air system and at high rates as the oxygen may be depleted, the discharge function at the cathode is taken over by the manganese dioxide. This means that such a battery should essentially have the capacity of zinc air battery when discharged at low rates, but is should have the pulse current capability of a manganese dioxide battery [34].

2.3.3 Aluminum air batteries

Aluminum air batteries are gaining a lot of attention after Li-air batteries because they have theoretical specific capacity of $1030 AhKg^{-1}$ which is second highest after Li-air ($1170 AhKg^{-1}$). Due to some disadvantages of Li-air batteries mentioned before, Al-air batteries have gained interest as battery material. Thermodynamically, a pure aluminum anode exhibits a potential of -1.66V (vs Hg/HgO) in saline and -2.35V(vs Hg/HgO) in aqueous solution. Besides the electrode processes on the Aluminum surface, the aluminum goes through formation or dissolution of an initial Al_2O_3 and $Al(OH)_3$ layer, three electron charge transfer process, formation of corrosion products like $Al(OH)_4^-$ and $Al(OH)_3$ and parasitic corrosion reaction which releases hydrogen [34].

The discharge reactions for the aluminum air cell are:

$$\text{Anode: } Al \longrightarrow Al^{+3}+3e$$

$$\text{Cathode:} O_2+2H_2O+4e^- \longrightarrow 4OH^-$$

$$\text{Overall: } 4Al+3O_2+6H_2O \longrightarrow 4Al\ (OH)_3$$

And the parasitic hydrogen generating reaction is:

$$Al+3H_2O \longrightarrow Al\ (OH)_3+3/2\ H_2$$

This side reaction causes corrosion and passivation of the aluminum surface leading to the battery failure. This thermodynamically favorable protective oxide film forms spontaneously on the surface when exposed to air and aqueous solution. This oxide layer leads to a positive shift of the corrosion potential and slow down aluminum activation [35, 36]. This is usually solved by using aluminum alloys for Al-air batteries and decreasing corrosion rate. Addition of alloying elements such as Ga, Ti, In, Sn, Zn, Bi, Mn and Mg have been adopted. Most commonly used anode materials in Al-air batteries are Al-Zn, Al-In, Al-Ga and Al-Sn [37-47]. Similarly, the other alloying elements help in improving the performance of AL-air batteries.

The outstanding performance of Al alloys in Al-air batteries can be attributed to comprehensive effect of each individual alloying component. Besides Al-alloys, the electrolyte also plays important role in function of the battery. The neutral electrolytes are attractive because of the low open circuit corrosion rates. These are used as portable reserve batteries. The seawater batteries are usually preferred for high energy output but they require high surface area. The alkaline electrolytes have higher conductivity and solubility for aluminum hydroxide compared to other electrolytes and could be used for high power applications [10].

2.3.4 Magnesium air batteries

2.3.4.1 History of Magnesium batteries

Magnesium air batteries are one of the metal air batteries which need to be explored more. High theoretical energy density and abundance in the earth makes these batteries potential candidates for future battery applications. The basic structure of Mg-air battery is given in Figure 2.3 [48]. It is composed of Mg or magnesium alloy as anode, an air cathode and neutral electrolyte.

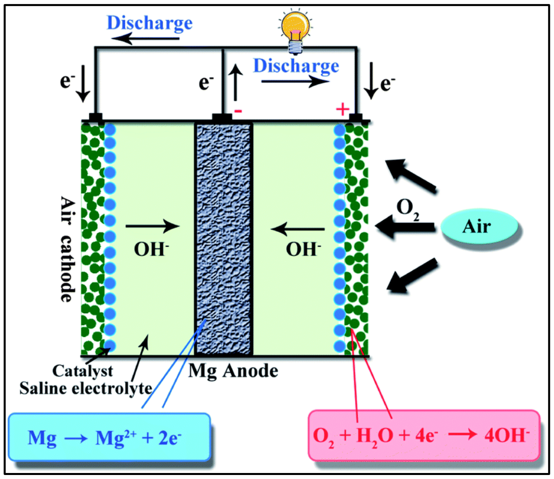

Figure 2.3: Schematic diagram of Mg-Air battery [48]

The reactions that occur in Mg-air batteries is given below:

$$\text{Anode: } Mg \longrightarrow Mg^{2+} + 2e$$

$$\text{Cathode: } O_2 + 2H_2O + 4e^- \longrightarrow 4(OH)^-$$

$$\text{Overall: } Mg + 1/2O_2 + H_2O \longrightarrow Mg\,(OH)_2$$

During the discharge process, the anode Mg is oxidized to Mg^{2+} producing two electrons while at cathode, the oxygen passes through the air cathode and is then reduced to OH^- by the reaction of water and electrons [49]. The theoretical voltage of the Mg-air battery is 3.1 V and the open circuit is about 1.6 V. Magnesium batteries have good theoretical energy density, has high reaction activity, light weight, has low toxicity and is abundant on the earth[50]. This makes Mg-air battery a potential candidate to use in battery application. Besides this, Mg-air batteries can be reused by replacing the spent Mg anode and electrolyte with fresh batch. Even though Mg-air battery has different advantages over other air batteries, its performance is still limited by several characteristics like self-corrosion or spalling in both storage and discharge state, limitation of the electronic conductivity due to coverage of discharge products on the surface and increase in hydrogen evolution reaction [51].

Different parts of Mg-air batteries are explained with strategies to overcome the issues are described in the following sections.

2.3.4.2 Magnesium anode

Magnesium alloys are utilized in engineering design mainly because of their high strength-weight ratio, excellent machinability and relatively low cost. The density of magnesium is 1.738 g/cm3 which is lower than iron (7.874 g/cm3) and aluminum (2.5 to 3.0 g/cm 3) of aluminum making it the lightest structural metal. [1], the famous structural metal. Magnesium is rarely used in a pure form and when alloyed with other material can have a good mechanical and corrosion properties. Light weight characteristics and wide availability make magnesium alloys suitable for mass production of components in automobile and aerospace industries. The increase in demand of magnesium in different applications has driven the development of magnesium and related technologies resulting in better availability of creep resistant and corrosion resistant magnesium alloys [2].

Magnesium anode and its alloys are susceptible to different types of corrosion. Major type of corrosion magnesium anode is susceptible is galvanic corrosion. Magnesium alloys are susceptible to galvanic corrosion due to poor design and flux contamination. Most of the alloys have presence of metals like iron, nickel or copper which has comparatively low hydrogen voltage. These can act as efficient cathodes for hydrogen evolution reaction and galvanic corrosion. Different experiments done by TONG et al, on different magnesium alloys like AM50 and AM60 showed that magnesium alloys act as anode and their corrosion rates increased when alloyed with steel brass and aluminum alloy [52]. Magnesium alloys undergo galvanic corrosion when alloyed with other metals so proper material selection and coatings should be done in order to reduce the galvanic corrosion.

The other type of corrosion that Magnesium and its alloys go through is pitting corrosion. This corrosion occurs at free corrosion potential of magnesium when expose to chloride ions a non-oxidizing medium [53].

The pits initiate at damages near the secondary phase particles when the passive film breaks. The secondary phase particles act as cathode and surround Mg matrix as anode after the film breaks and then leads to the pitting corrosion. When immersed in NaCl solution, the CL^- ions will be absorbed around the secondary phase particles. When the passive film reaches breakdown potential, the alpha of matrix acts an anode compared to secondary particles and starts to dissolve. This forms a corrosion nucleus around secondary particle and finally develops in corrosion pit [54].

Intergranular corrosion occurs at grain boundaries due to the precipitation of secondary phase. The alloys wit intermetallic phases are highly susceptible to intergranular corrosion. But MAKER et al. insisted that true intergranular corrosion did not occur in Mg alloys because the phases at the grain boundaries are almost cathodic to the grains. Corrosion tends to be concentrated adjacent to the grain boundary until spalling occurs [55, 56]. But some of the recent studies found out the occurrence of intergranular corrosion in Mg alloys. Valente noticed intergranular corrosion in WE43 magnesium alloy [57]. The other researcher, GHALI et al also showed the localized attack of Mg alloy at the grain boundaries in presence of mild corrosive media [58].

Filiform corrosion usually occurs on steel, aluminum and magnesium. It is the result of active galvanic sites throughout the surface. Dexter showed that the filiform corrosion of magnesium is driven by oxygen concentration between the head and tail which contradicts magnesium corrosion being relatively insensitive to the oxygen concentration differences [59].

Die cast Magnesium alloys are more susceptible to SCC than rapidly solidification and semi solid cast alloys [60].SCC are attributed to one of two groups of mechanisms: continuous crack propagation by anodic dissolution at the crack tip or discontinuous crack propagation by a series of mechanical fractures at the crack propagation due to mechanical crack tip. There are two types of SCC based on the fracture morphology of samples, transgranular SCC and intergranular SCC. TGSCC is major type of SCC which occur mainly due to hydrogen evolution [61].

Magnesium is susceptible to different corrosions described above. This leads to high corrosion rate of pure magnesium. The high corrosion rate of pure magnesium will affect the life cycle of the battery as it will be used up in a very short time. One of the strategies to overcome the self-corrosion of the pure magnesium is to alloy with appropriate metals to form efficient magnesium alloys.

Magnesium alloys can be divided into zirconium-free and zirconium-containing magnesium alloys. Magnesium can be alloyed with aluminum is a major alloying element with minor elements such as manganese, silicon, and zinc and form zirconium free magnesium alloys. The examples of magnesium alloys in this category are aluminum-manganese such as AM20, AM50, AM60, aluminum-silicon such as AS21, AS41, and aluminum-zinc, the most widely used, such as AZ31, AZ81, AZ91. Aluminum content can be varied to achieve desirable properties; for example, low aluminum content provides good ductility, 6 wt% of aluminum provides best mechanical properties [1], and high aluminum content provides high strength and good castability [3]. The other alloy magnesium-zinc-copper alloys similar to magnesium-aluminum are developed to get ductility and stability. Magnesium-zinc-zirconium alloys are another type of commercial magnesium alloys. Rare earth elements improve strength at elevated temperature and creep resistance of magnesium alloys [4].

Recent results demonstrated that the addition of REs is the most promising method to weaken the texture and improve the deformability of magnesium alloys [62-65]. Rare earth elements when added to Magnesium enhance the mechanical properties and good corrosion resistance. The addition of Zn in the alloy helps in providing a maximum solubility of 6.2wt%. When RE is added to Mg-Zn to form Mg-Zn-RE alloys such as Mg-Zn-Gd or Mg-Zn-Y, the resulting alloy exhibited excellent corrosion resistance properties [66, 67].

EV31A (Elektron 21) is one of the magnesium rare earth alloys used in the project. EV31A (Mg-Zn-Gd-Nd-Zr) alloy is a heat treatable magnesium cast alloy that can be used up to 200^{o}C for automobile and aerospace applications. It nominally has (in wt %) 0.2%-0.5%Zn, 2.6%-3.1%Nd,1.0%-1.7%Gd and saturated amount of Zr as alloying additions. Zr has a calculated solubility of about 0.76at % in liquid MG and about 0.2% at 400^{o}C.The maximum solid solubility of Zn at eutectic temperature is 2.4 at% and decreases to about 0.1at% at room temperature. The identified secondary phases in the Mg-Zn-Zr system are MgZn, Mg_7Zn_3,Zn_2Zr_3, ZnZr,$(Zn,Mg)_2Zr$ and $Zn_2(Mg,Zr)$(source). Out of these, Zn_2Zr_3 phase is most likely to be present in the EV31A alloy [68]. The terminal solid solution of ND in Mg is considered to be 0.7at% at its eutectic temperature(822K) and the secondary phases that are in equilibrium with the solid solution are $Mg_{41}Nd_5$,Mg_3Nd,Mg_2Nd, MgNd and $Mg_{12}Nd$[69]. The Mg_2Nd phase is considered to be metastable since only the quenched sample contained this phase and not the annealed ones [68]. The terminal solid solubility of Gd in Mg is reported to be 23.49wt% at 548^{o}C and the secondary phases of the Mg-Gd binary system are Mg_5Gd, Mg_3Gd, Mg_2Gd and MgGd. Addition of Nd and Gd together helps improve the age hardening response as the solubility of Gd is reduced with the incorporation of Nd [69]. Zinc is also considered to enhance the age hardening response and creep strength of Mg-Gd alloys [70]. In a MG-Nd-Gd system, addition of Zn can delay averaging process at 250^{o}C and increase the hardness [71].

Mg-RE alloy Electron717 (ZE10A, UNS M11600) has a nominal composition of 1.2wt % Zn, 0.25wt% Zr, <0.5%Nd, 0.007wt%Mn, 0.004wt %Fe,0.001wt%Ni and balanced Mg. Since it is Mg-Zn-Zr system, the secondary phases identified in this alloy is same as EV31A.The addition of Zr makes this alloy more castable, corrosion resistant and could be used in automobile industry.

The formation of passive layer affects the corrosion behavior of magnesium alloys. The magnesium alloy also goes through negative difference effect which is accompanied by strong hydrogen evolution. The hydrogen evolution is attributed to the presence of film free regions inside the pits. Pits occur due to inability of magnesium to form a uniform layer like aluminum. This increases the film free surface with anodic polarization must overcompensate the decrease of the cathodic current density by anodic polarization. This effect is also seen in aluminum alloys and ferrous materials but is more complex in magnesium alloys because the hydrogen gas results from the partial reaction occurring during localized corrosion inside the pits as well as from the cathodic reaction on the surface outside the pits [72].

Thus, it is important to discuss about the corrosion mechanism of the Mg and its alloys to be used as anode in the batteries. In the Pourbaix diagram of Mg-water system at 25^{O}C and is thermodynamically stable below -2.37V with large pH range. Unfortunately, the area is below the region of water stability. Mg^{2+} is the stable substance in the pH range from 0 to 11above which $Mg(OH)_2$ is stable. Consequently, in neutral and acidic aqueous environment, Mg spontaneously converts to Mg ions. These further react with water through an electrochemical reaction to produce magnesium hydroxide and hydrogen gas involving micro galvanic coupling between cathodic areas and anodic areas. This process is the corrosion of Mg with the following three parts [72]:

Anode: $Mg \longrightarrow Mg^{2+}+2e$

Cathode: $2H_2O+2e^- \longrightarrow H_2+2OH^-$

Layer: $Mg^{2+}+2OH \longrightarrow Mg(OH)_2$

Overall: $Mg+2H_2O \longrightarrow Mg(OH)_2+H_2$

As seen from the above equations, the hydrogen evolution reaction causes the rise in corrosion of Mg. Besides HER, the other effect Negative Differential Effect also causes the corrosion reaction [73]. The more detailed corrosion process of Mg which produces hydrogen is given in the following equations[74] :

$$Mg + H_2O \rightarrow Mg(OH_{ads})(H_{ads})$$

$$Mg(OH_{ads})(H_{ads}) \rightarrow Mg(O_{ads}) + H_2$$

$$Mg(OH_{ads})(H_{ads}) + H_2O \rightarrow Mg(O_{ads})_2 (H_{ads})_2$$

$$Mg(O_{ads})_2 (H_{ads})_2 \rightarrow Mg(OH_{ads})_2 +H_2$$

It is very difficult concept to understand why the corrosion rate increases on Mg-anode during oxidation. This causes the corrosion rate to increase during the battery discharge and reduce the efficiency of the battery. The negative differential effect is where huge amount of hydrogen is generated as a result of the cathodic reaction balancing rapid anodic dissolution during open circuit exposure in aqueous solution. Generally the corrosion reaction is either anodic or cathodic process. For most of the metals such as iron, zinc or steel, when the applied potential increases, the anodic current rises and cathodic current decreases simultaneously. But in case of Mg, the behavior is quite different [74]. Moreover, the rate of the partial cathodic reaction increases with applied increased anodic potential [72]. From the figure 2.4, it is seen that anodic current I_{Mg} and cathodic current I_H both rise with an increase of applied potential. This is called the negative difference effect and the increase in NDE accelerates the corrosion of Mg. This phenomenon represents two processes which are persistent cathodic reaction and anodic dissolution catalyzed cathodic reaction [73]. The anodic kinetics of Mg dissolution is weakly polarizable as it represents a low Tafel slope compared to cathodic reaction which has a very high tafel slope and high polarization rate which effects the corrosion of Mg [72].Thus, the hydrogen evolution reaction can be reduced by addition of micro alloying element arsenic (As) as cathodic poison to suppress cathodic reaction and cathodic activation of Mg. Microalloying addition of arsenic (As) was reported to render remarkable corrosion resistance by significantly suppressing hydrogen evolution [74]. Since the alloying additions such as Pb and As are toxic, more environmentally friendly elements that render similar beneficial effects have been recently investigate. To that effect, Liu et al recently reported microalloying additions of Ge, Sb, Pb, Sn and Bi that markedly decrease the cathodic activation and improved the corrosion resistance [75]. Alloying with Sn not only increase the hydrogen overpotential and decrease the self-discharge but also helps peel off the corrosion products that result in increased discharge voltage at high current density [76]. The Mg-Al-Pb allohy anode shows low anodic efficiency, low stability at OCP and detachment of metal pieces even at low anodic current densities [77].Rare earth elements are added to the Mg-Al-Pb and Mg-Li-Al alloys to improve the performance of Mg-Air batteries [78,79].

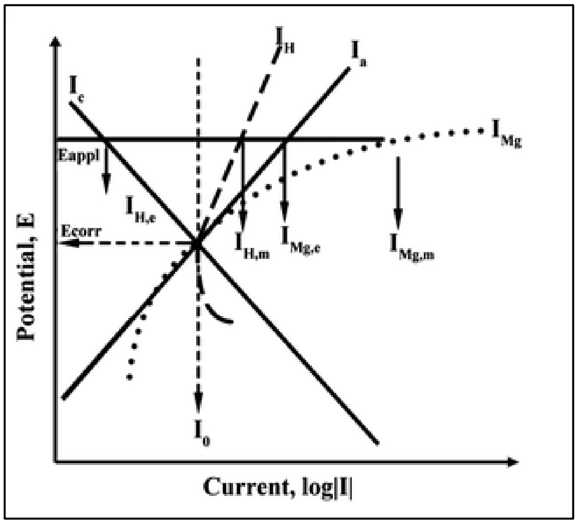

Figure2.4: Schematic of NDE of Mg anode [73]

2.3.4.3 Electrolyte

Electrolyte also plays huge role in battery performance besides anode. Neutral alkaline solutions are used in Mg air battery with pH ranging from 6.5-7.5. Mg has a higher resistance in alkaline solution than in acidic or alkaline solution.

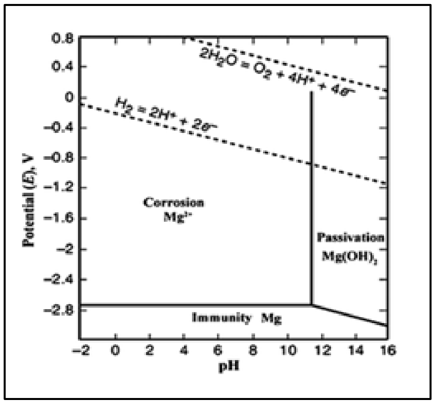

Figure 2.5: Pourbaix diagram of Mg

From the figure 2.5, it is seen that Mg goes through corrosion when the potential is above -2.8 and pH less than 11. The hydrogen evolution reaction and corrosion rate of Mg can be controlled by increasing the pH level above 11. The reason for high corrosion resistance of MG in the alkaline solution is due to the partial formation of $Mg(OH)_2$ film on the electrode. Even though the film could protect the anode from further corrosion, this will also prevent further reaction of the anode and stop the battery function. Thus, a neutral electrolyte is used in Mg-air batteries to ensure the corrosion rate is controlled and long term function of the battery. Since, the Mg-air battery usually uses seawater to function, 3.5 wt. percent NaCl or 0.6 M NaCl is used as electrolyte in the battery. But in addition to NaCl, the other electrolytes like Na_2SO_4 shows promising performance as electrolyte. $NaNO_3$ has comparatively more resistance to corrosion of Mg compared to NaCl and Na_2SO_4. It has been found that Cl^- and SO_4^- are more likely to attack Mg and thus lead to high corrosion rates while NO_3^- ions do not attack magnesium to same extent.

In addition to the electrolytes, addition of inhibitors like stannates, quaternanry ammonium salt, dithiobiuret etc. can suppress the HER and increase the efficiency of the battery [74].

2.3.4.4 Air Cathode

Successful operation of Mg-air battery also depends on an effective air cathode. Researches on fabrication of an effective air cathode with better catalyst and low cost are equally as important as the research on anode. The air cathode consists of diffusion layer, catalyst layer current collector and waterproof layer. The gas diffusion layer has high porosity and electronic conductivity, catalyst layer is composed of active catalyst for oxygen reduction reaction. The over potential of the air cathode is caused by the sluggish kinetics of the ORR which leads to bad performance of the battery [74].

Thus the efficiency of the battery is dependent on all the components of the cell, so researches are still being conducted on each aspect to come up with the best solution to increase the efficiency of the Mg-Air batteries.

References

1. American Society for Metals. (1986). *Metals Handbook Desk Edition. Metals.* Park, OH: American Society for Metals.
2. Rand, D.E., (1979).*Battery Systems for Electric Vehivels:State of Art Review.* J.Power Sources,101
3. Liu, Y., Sun, Q., Li, W. Adair, K.R., Li, J., & Sun, X. (2017) *A Comprehensive Review on Recent Progress in Aluminum-Air Batteries.* Green Energy & Environment, 246-277
4. Lee J.S., Kim S.T., Cao R., Choi N.S., Liu M., Lee K.T.,& Cho J. *Metal-Air Batteries with High Energy Density:LI-Air versus Zn-Air.* Advanced Energy Materials.
5. American Society for Metals. (1986). *Metals Handbook Desk Edition. Metals.* Park, OH: American Society for Metals.
6. G. Song and A. Atrens, *Adv. Eng. Mater*.(2003) **5**, 837–858
7. W. Yang, S. Yang, G. Sun and Q. Xin, *Chin. J. Power Sources*, 2005, **29**, 182–186
8. Liu, Y., Sun, Q., Li, W. Adair, K.R., Li, J., & Sun, X. (2017) *A Comprehensive Review on Recent Progress in Aluminum-Air Batteries.* Green Energy & Environment, 246-277
9. Lee J.S., Kim S.T., Cao R., Choi N.S., Liu M., Lee K.T.,& Cho J. *Metal-Air Batteries with High Energy Density: Li-Air versus Zn-Air.* Advanced Energy Materials.
10. J. A. Zhang , W. Xu , X. H. Li , W. Liu , J. Electrochemical Soc. (2010), 157 , A940.
11. J. Kumar , B. Kumar , J. Power Sources (2009) , 194 , 1113
12. J. G. Zhang , D. Y. Wang , W. Xu , J. Xiao , R. E. Williford , J. Power Sources (2010), 195, 4332.
13. T. Ogasawara , A. Debart , M. Holzapfel , P. Novak , P. G. Bruce , J. Am. Chem. Soc. (2006) , 128 , 1390 .

14. C. O. Laoire , S. Mukerjee , K. M. Abraham , E. J. Plichta , M. A. Hendrickson , J. Phys. Chem. C 2009 , 113 , 20127 .
15. C. O. Laoire , S. Mukerjee , K. M. Abraham , E. J. Plichta , M. A. Hendrickson , J. Phys. Chem. C 2010 , 114 , 9178
16. Y. G. Wang , H. S. Zhou , J. Power Sources 2010 , 195 , 358 .
17. Y. G. Wang , H. S. Zhou , Chem. Commun. 2010 , 46 , 6305
18. B. Kumar , J. Kumar , R. Leese , J. P. Fellner , S. J. Rodrigues , K. M. Abraham , J. Electrochem. Soc. 2010 , 157 , A50
19. Arafat, R. M., Xiaojian, W. & Cuie, W. High Energy Density Metal-Air Batteries: A Review. *J. Electrochem. Soc.* **160**, A1759–A1771 (2013).
20. Narayanan, S. R. *et al*. Materials challenges and technical approaches for realizing inexpensive and robust iron-air batteries for large-scale energy storage. *Solid State Ion.* **216**, 105–109 (2012).
21. Clark, S., Latz, A. & Horstmann, B. A review of model-based design tools for metal-air batteries. *Batteries* **4** (2018)
22. Li Y, Dai H (2014) Recent advances in Zinc-air batteries. Chem Soc Rev 43: 5257.
23. Rahman MA, Wang X, Wen C (2013) High energy density metal-air batteries: A review. J Electrochem Soc 160: A1759–A1771.
24. Rahman MA, Wang X, Wen C (2013) High energy density metal-air batteries: A review. J Electrochem Soc 160: A1759–A1771.
25. Nixon DB Electric vehicle having multiple replacement batteries: US (1994), US 5542488 A.

26. Siahrostami, S. *et al*. First principles investigation of zinc-anode dissolution in zinc-air batteries. *Phys. Chem. Chem. Phys.* **15**, 6416–6421 (2013).
27. W. H. Zhu, B. A. Poole, D. R. Cahela, B. J. Tatarchuk, J. Appl. Electrochem., (2003)
28. T. P. Dirkse, D. J. Kroon, J. Appl. Electrochem., 1971
29. M.L. Doche, J.J. Rameau, R. Durand, F. Cattin. Corrosion Science41(1999),805-826
30. L. Fan, H. Lu, J. Power Source, 284(2015), 409-415
31. M. Pino, D. Herranz, J. Chacon, E. Fatas, P. Ocon. J. Power Sources (2016), 296-302
32. A.R. Despic, D.M. Drazic, M.M. Purenovic, N. Cikovic, J. Applied Electrochem 6 (1976) 527-542
33. H.A. E. Shayeb, E. M.A.E. Wahab, S.Z.E. Abedin, J. Applied Electrochem 29(1999)473-480
34. S.Z.E. Abedin, F.Endres, J. Appl. Electrochem. 34(2004)1071-1080
35. L. Smoljko, S. Gudic, N. Kuzmanic, M. Kliskic, J. Applied Electrochem.42(2012)969-977
36. S. Gudic, I. Smoljko, M. Kliskic, Material Chem Phys.121(2010)561-566.
37. W. Wilhelmsen, T. Arnesen, Hasvold, N. J. Storkersen, Electrochimica Acta 36(1991) 79-85
38. Zinc helps to reduce the hydrogen evolution on Al anodes by enhancing the HER potential and thus relieveing the anode degradation
39. M. Pino, J. Chacon, E. Fatas, P. Ocon, J. Power Sources 299 (2015) 195-201
40. Z. Sun, H. Lu, J. Electrochem. Society 162(2015) A1617-A1623
41. Z. Tianran, T. Zhangliang and C.Jun, *Magnesium-air Batteries: From Principle to Application.* Royal Society of Chemistry (2014)1, 196-206.

42. W. Yang, S. Yang, G. Sun and Q. Xin, Chin. J. Power Sources, (2005) 29, 182–186
43. B. Peng, J. Liang, Z. Tao and J. Chen, J. Mater. Chem., (2009) 19, 2877–2883
44. B. A. Shaw, *Corrosion Resistance of Magnesium Alloys*, ASM International (2003)
45. TONG Zhen-song, ZHANG Wei, L1 Jiu-qing, CHENG Fei. Initial laws of atmospheric galvanic corrosion for magnesium alloys [J]. The Chinese Journal of Nonferrous Metals, 2004, 14(4): 554-561. (in Chinese)
46. SONG G ATRENS A. Corrosion mechanisms of magnesium alloys [J]. Advance Engineering Materials, 1999,l: 11-33.
47. ZENG Rong-chang, ZHOU Wangqiu, HAN En-hou, KE Wei. Effect of pH value on corrosion of as-extruded AM60 magnesium alloy [J]. Acta Metallurgica Sinica, 2005,44(3): 307-3 1 1 .(in Chinese)
48. MAKER G L, KRUGER J. Corrosion of magnesium [J]. International Material Review, (1993) 38: 138-153.
49. SONG G ATRENS A. Corrosion mechanisms of magnesium alloys [J]. Advance Engineering Materials (1999)l: 11-33.
50. VALENTE T. *Grain boundary effects on the behavior of WE43 magnesium castings in simulated marine environment*, Journal of Materials Science Letters, 2001,20: 67-69.
51. GHALI E, DIETZEL W, KAINER K U. *General and localized corrosion of magnesium alloys: a critical review [J]*. Journal of Materials Engineering and Performance (JMEPEG), (2004) 13(1): 7-23
52. Dexter S C. Metals Handbook (Vol.l3). 9th ed. OH: ASM International (1987). 106.

53. Wmzer N, Atrens A, Song C, Ghali E. Dietzel W, Kainer K U, Hort N, Blawert C. *A critical review of the stress corrosion cracking (SCC) of magnesium alloys [J]*. Advanced Engineering Materials (2005), 7(8): 659-693
54. William K, Miller. Stress-corrosion Cracking [MI]. Ohio: ASM (1993).251.
55. N. Standford, D. Atwell, A. Beer, C. Davies, M. R. Barnett, Scr. Matter., 59 (2008), 772-777
56. N.Standford, M. Barnett Scr.Mater.,58(2008), 179-181
57. J. Bohlen, M. R.., Nurnberg, J. W. Senn, D. Letzig, S.R. Agnew Acta Mater., 55(2007), 2101-2112
58. M.R. Barnett, A. Beer, D. Atwell, C.H.J. Davies, T. Abbott, S.R. Agnew, M.R. Neelamegham, E.A. Nyberg, W. H. Sillekens (Eds.), Magnesium Technology 2010, The Minerals, Metals and Materials Society (TMS), Seattle, Washington, USA(2010), 353-357
59. G. Yuan, Y. Liu, W. Ding, C. Lu. *Effects of extrusion on the microstructure and mechanical properties of Mg-Zn-Gd alloy reinforced with quasicrystalline partielces* . Mater Science Engineering A, 474(1) (2007), 348-354
60. M. Yamasaki, K. Hashimoto, K. Hagihara, Y. Kawamura. *Effect of multimodal microstructure evolution on mechanical properties of Mg-Zn-Y extruded alloy.* Acta Mater,59 (9)(2011), 3646-3650
61. Li C.S., Sun Y., Gbert F.,& Chou S.*Current Progress on Rechargeable Magnesium-Air Battery.* Advanced Energy Materials.

62. *Protecting Magnesium alloys from corrosion* [web journal]. Retrieved from https://www.thefabricator.com/article/metalsmaterials/protecting-magnesium-alloys-from-corrosion
63. Friedrich, H. E., & Mordike, B. L. (Eds.). (2006). *Magnesium technology: metallurgy, design data, applications.* Verlag Berlin Heidelberg, Germany: Springer.
64. *Introduction to the Rare Earths* [PDF document]. Retrieved from https://www.liverpool. ac.uk/~sdb/Research/Chapter1.pdf
65. Chu, P. W., & Marquis, E.A. (2015) Linking Microstructure of a Heat-Treated WE43 Mg Alloy with its Corrosion Behavior. *Corrosion Science*, 101, 94 - 104.
66. Weber, C.R., Knornschild, G., & Dick, L.F.P.(2003). *The negative-difference effect during the localized corrosion of magnesium and of the AZ91HP alloy.* Journal of Brazilian Chemical Society.
67. Kirkland, N. T., Williams, G. & Birbilis, N. Observations of the galvanostatic dissolution of pure magnesium. *Corrosion Science* **65**, 5–9, doi: 10.1016/j.corsci.2012.08.029 (2012)
68. Frankel, G. S., Samaniego, A. & Birbilis, N. Evolution of hydrogen at dissolving magnesium surfaces. *Corrosion Science* **70**, 104–111, doi: 10.1016/j.corsci.2013.01.017 (2013).
69. Weber, C.R., Knornschild, G., & Dick, L.F.P.(2003). *The negative-difference effect during the localized corrosion of magnesium and of the AZ91HP alloy.* Journal of Brazilian Chemical Society.
70. Bland, L. G., King, A. D., Birbilis, N. & Scully, J. R. *Assessing the Corrosion of Commercially Pure Magnesium and Commercial AZ31B by Electrochemical*

Impedance, Mass-Loss, Hydrogen Collection, and Inductively Coupled Plasma Optical Emission Spectrometry Solution Analysis. Corrosion **71**, 128–145, doi: 10.5006/1419 (2015).

71. G. Song and A. Atrens, *Adv. Eng. Mater.*, 2003, **5**, 837–858
72. B. W. Jensen, M. Gaadingwe, D. R. Macfarlane and M. Forsyth, *Electrochim. Acta*, 2008, **53**, 5881–5884
73. D. Wang, Y. Yu, H. L. Xin, R. Hovden, P. Ercius, J. A. Mundy, H. Chen, J. H. Richard, D. A. Muller,F. J. Di Salvo and H. D. Abruña, Nano Lett. (2012) **12**, 5230–5238
74. N. Birbilis, G. Williams, K. Gusieva, A. Samaniego, M.A. Gibson, H. N. McMurray, Elecrochemistry Communication 34,295(2013)
75. R. L. Liu, J. R. Scully, G. Williams, N. Birbilis, Electrochimica Acta 260, 184 (2018)
76. H. Xiong, K. Yu, X. Yin, Y. Dai, Y. Yan, H. Zhu, Journal of Alloys and Compounds 708, 652 (2017)
77. N. Wang, R. Wang, C. Peng, Y. Peng, Corrosion Science, 81, 85 (2014)
78. Y. Feng, W. Xiong, J. Zhang, R.Wang, N. Wang, Journal of Material and Chemical A4, 8658 (2016)
79. D. Cao, L. Wu, G. Wang, Y. Lu, Journal of Power Sources, 183,799 (2008)

Chapter 3: Experimental Procedure

3.1 Material Preparation

Two-millimeter-thick sheets of Mg-RE alloy ZE10A (Elektron 717, Magnesium Elektron North America, Inc.,) and EV31A (Elektron 21, Magnesium Elektron North America, Inc.,) were received in the mill annealed condition. Rectangular coupons of 20 x 25 mm^2 were cut from the sheet. Commercial purity magnesium was obtained in the form of 2 mm thick sheet and 20 x 25 mm^2 coupons were machined out of the sheet stock. All three samples were received in as received condition and no heat treatment was done on them. All these specimens were metallographically polished using SiC emery paper down to 1200 grit in dry condition and wet polished using 0.5 μm size alumina suspension with grinding machine Twinprep 3 created by Allied High Tech Productions as shown in figure 3.1. The polished specimens were ultrasonically cleaned in methanol and dried in nitrogen stream. For metallographic inspection, these specimens were etched with a solution made up of 0.1 M nitric acid and ethylene glycol mixed in 3:1 ratio for 5-10 seconds.

Figure 3.1: Grinding and Polishing Machine

3.2 Electrochemical measurements

The specimens were weighed before and after the electrochemical experiments. A flat cell made of PTFE was used for running the electrochemical experiments. The specimen was secured outside the PTFE container exposing 1 cm^2 surface area of the specimen to the electrolyte. A spiral of Pt wire (2.5cm^2 surface area) as counter electrode and the reference electrode was Ag/AgCl in saturated KCl (199 mV vs SHE). The electrolytes used were: 0.6 M of NaCl, 0.5M of $NaNO_3$ and 0.1 M of Na_2SO_4. Figure 3.2 shows the schematic of the setup to carry out the electrochemical experiments.

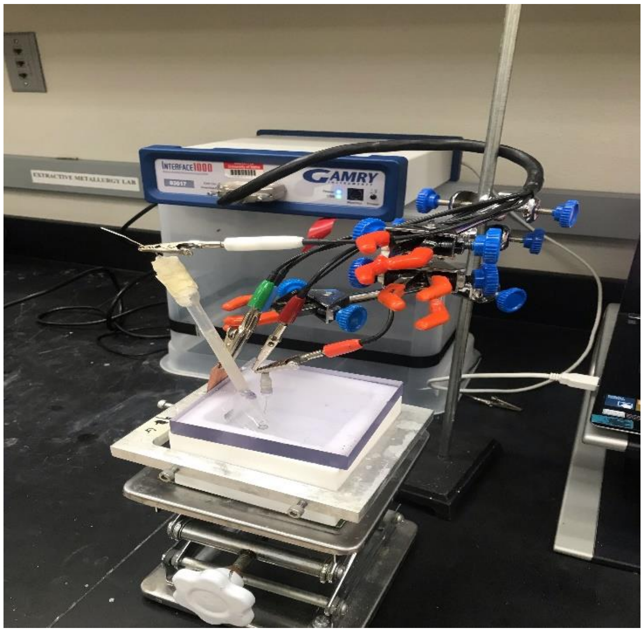

Figure 3.2: Cell setup for Electrochemical Measurements

Linear polarization plots were obtained by scanning the potential in the range of -0.025V to 0.025V vs. open circuit potential (OCP) to obtain the polarization resistance values (R_p). Anodic and cathodic Tafel slopes were obtained by constructing Tafel plots by scanning the potential from -0.25 V to 0.25 V versus OCP. Anodic polarization was performed by scanning the potential from open circuit potential to a potential until 5 mA/cm^2 current density was recorded at a rate of 1 mV/s. Electrochemical impedance spectroscopy was carried out by superimposing a 10 mV AC signal on the last recorded OCP and scanning the frequency from 10000 Hz to 0.01Hz. Tafel slopes and corrosion current density were obtained from the electrochemical technique. A computer controlled potentiostat (Gamry Instruments, Model: Reference 1000, Gamry Framework Version 6.04, and Gamry Echem Analyst Version 6.04) was used to carry out all the electrochemical experiments as shown in figure 3.3.

Figure 3.3: Gambry Instrument

3.3 Hydrogen Evolution Measurement

Galvanostatic hydrogen evolution test was carried out to measure the rate of hydrogen collected per second. Faradaic efficiency was calculated and compared for all three samples. Hydrogen evolution increased with the increase in voltage and current when the potentiostatic and galvanostatic tests were carried out. According to Tafel equation to describe the hydrogen evolution rate at Mg surface:

$$i_{HER} = i_o e^{(-(E-E0)/b)}$$

Where, i_{HER} is the current density of hydrogen evolution at any potential, i_o is the exchange current density for hydrogen evolution reaction on Mg surface and b is the Tafel Slope.

Hydrogen evolution was measured using the arrangement shown in Fig. 1 during anodic polarization of the specimens under both potentiostatic and galvanostatic conditions. The electrochemical cell was made of PTFE and had an opening with O-ring at the bottom to accommodate the specimen. A three-electrode configuration was used with Pt-wire spiral as counter electrode, and an Ag/AgCl in saturated KCl reference electrode. This design is similar to the one reported by King et al, an inverted glass burette having a funnel at the end was placed above the specimen and the hydrogen evolved from the specimen was collected. Before start of the experiments, the electrolyte column present in the burette was pre-saturated with hydrogen by cathodically polarizing a platinum wire electrode inserted into the burette to –1.5 $V_{Ag/AgCl}$ before polarizing the magnesium alloy specimens. The polarization of auxiliary Pt wire was stopped when the electrolyte column in the burette was pushed down by the collection of hydrogen to a pre-determined reading. The least count of the burette was 0.1 ml. After hydrogen pre-charging, the Pt wire was removed from the burette, and the specimen was connected to the potentiostat. Galvanostatic tests were performed at eight different current density; -1mA, -10mA, -20mA, -100mA, 1mA, 10mA, 20mA and 100mA and hydrogen was collected at each current density. Each experiments were run until stable data of hydrogen evolution was recorded. The total charge consumed for hydrogen collection is calculated and then the faradaic efficiency for the system is calculated using the relation: $Q_{total} = Q_{Hydrogen} + Q_{i\ net\ anodic}$.

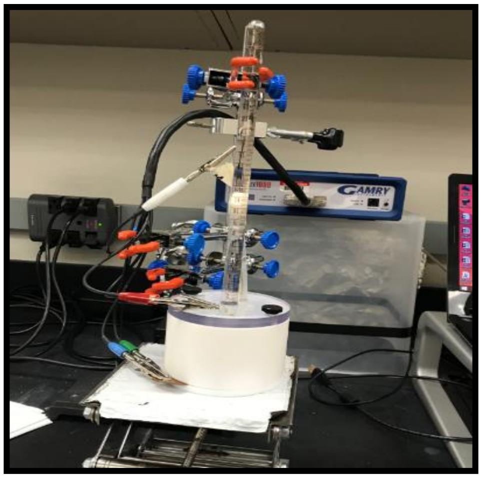

Figure 3.4: Setup for Hydrogen Collection

3.4 Calculation of Total Charge from HER

The total charge was set at 3600mA.sec and galvanostatic test was run at four different anodic currents: 1mA, 10mA, 20mA and 100mA for 3600secs, 360secs, 180secs and 36 secs respectively. The amount of hydrogen collected in this period was converted to charge.

Mathematical steps of calculating the total coulomb of charge is given below:

- Let x be the liters of hydrogen collected in 1 second. Then,
- x liters of H_2 * (1mole of H_2/22.4 liters of H_2) = y moles of H_2
- 2 moles of e^- is required to produce one mole of hydrogen gas so,
- y moles of H_2 * (2 moles of e^-/1 mole of H_2) = z moles of e^- is required for production of y moles of H_2 gas.
- z moles of e^- * (1F/1 mole of e^-) = m F
- m F * (96485C/1F) = n C where n is the total charge used up to produce x liters of hydrogen in one second.

3.5 Fabrication of Cathode

Air cathode was fabricated in the lab on nickel mesh. A nickel mesh of dimension 41.5x 35.3 mm^2 was cut and used as current collector. 0.6 grams of manganese dioxide was mixed with 0.03 grams of activated carbon and was bound together with PTFE binder. The mixture was then applied on the nickel mesh covering the area of 33.7x35.3mm^2. Both sides of the current collector was covered with a thin layer of Manganese dioxide and carbon mixture. The fabricated cathode was heated in box furnace at 370^{o}C for thirty minutes.Figure1 shows the lab fabricated air cathode for the battery.

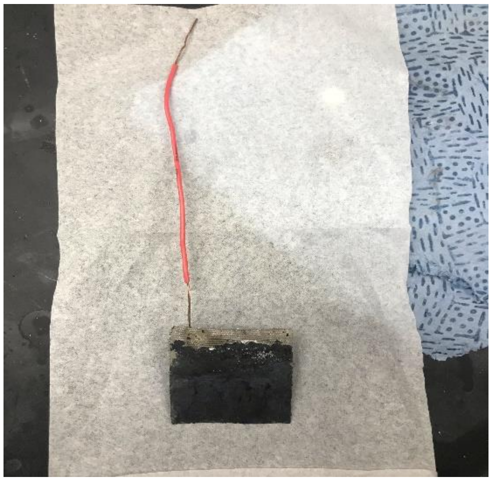

Figure 3.5: Air Cathode

3.6 Battery set up and Discharge Test:

The battery was set up in the lab on a simple cell. In the Mg air battery, discharge performance was done using a self-designed battery testing system as shown in figure 3.6. The battery was assembled in a simple two electrode cell system with anodic exposed area of 1cm^2. The electrolyte used was 0.6M NaCl. The discharge properties of cell with ZE10A and EV31A was measured and then compared with the properties of pure magnesium. The discharge properties of the cell was measured in galvanostatic conditions at 1mA/cm^2, 10mA/cm^2 and 20mA/cm^2 current density in 0.6M NaCl for three hours was measured in order to investigate the discharge performances of magnesium anode for both long term low power and short term high power battery system.

Additionally, the discharge morphologies were observed using scanning electron microscopy.

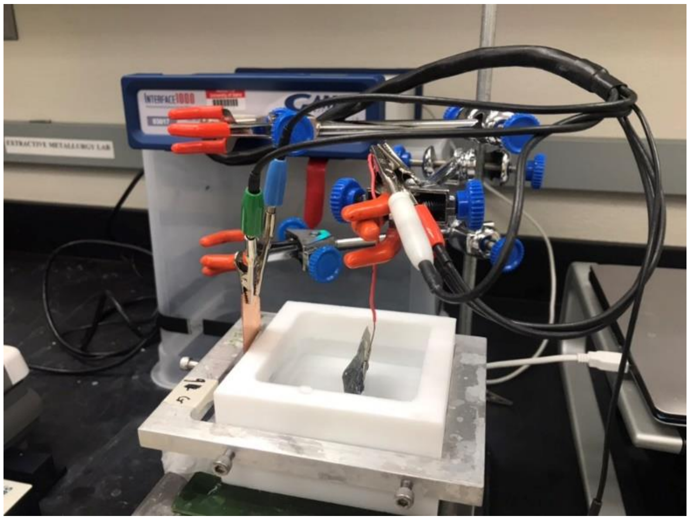

Figure 3.6: Battery Setup for Discharge Testing

Chapter 4: Results and Discussions

4.1 Microstructural Characterization

Figure 4.1 (a) shows the microstructure of commercial purity Mg equiaxed grains of average grain size of about 80 micrometer could be observed. The width of grain boundaries of Mg was longer than that observed in other two alloys. This implied that impurity elements segregated possibly along the grain boundaries. Most of the impurities present in the commercial purity such as Fe, Zr etc. are cathodic to the Mg matrix and therefore increase the corrosion of Mg in the region adjacent to the impurities by micro galvanic coupling [1]. Fig 4.1(b) shows the microstructure of EV31A alloy in solution treated condition. The solution treatment was carried at 525°C for 8 hours in argon atmosphere. Presence of discrete secondary phase particles could be observed even in the solution treated condition. These particles were identified as Zr- rich phase, MG_5Nd or Mg_7Zn_3[2]. The average grain size of EV31A was about 60 micrometer. Fig 1(c) shows the microstructure of ZE10A in solution treated condition. Discrete population of secondary phase particles could be observed along the grain boundaries and inside the grain as well in this specimen. Mg-Zn-Zr alloy typically contains α-Mg, α-Zr-rich phase and MG_xZn_y phases [3]. The volume fraction of secondary phases in a 1.87Zn, 0.54Zn Mg alloy was reported to be around 0.18%. Addition of Nd to Mg-Zn-Zr alloy results in formation of new ternary eutectic phases, denoted as T phases [4,5]. The stoichiometry of T-phases in Mg-Zn-Zr-Nd alloy with 2Zn,0.5Zr and 0.2 Nd could be given as $Mg_{60}Zn_{32}Nd_8$ and when the Nd content increased the stoichiometry of T phase was given as $Mg_{35}Zn_{40}Nd_{25}$[4] the volume fraction of secondary phases increased to about 1% with Nd addition.

Based on the Kelvin probe studies Cai et al showed that the Zr- rich and Mg Zn phases were cathodic to the Mg- solid solution in the simulated body fluid (SBF); whereas, the T-phases $MG_{60}Zn_{32}Nd_8$ and $Mg_{35}Zn_{40}Nd_{25}$ were anodic to the Mg-solid solution. Therefore the T-phases would dissolve in preference to the Mg-matrix [4]. Therefore, the dark spots observed in the micrograph could be associated with the dissolved T-phases.

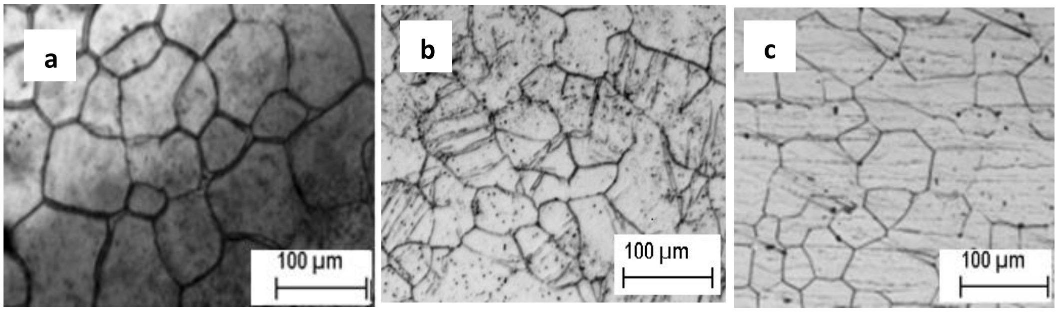

Figure 4.1 Optical microstructure of the specimens: (a) Commercial purity Mg, (b) ZE10A, and (c) EV31A (solution treated).

4.2 Electrochemical Measurements

Figures 4.2(a)-(c) show the anodic polarization behaviors of the Mg, ZE10A and EV31A alloy specimens in the 0.6M NaCl, 0.1M Na_2SO_4 and 0.5M $NaNO_3$ solutions, respectively. These plots are presented as recorded without any IR drop corrections. Therefore, significant polarization was observed at high current densities. It is reported that Mg and its alloys typically exhibit a non-polarizable or weakly polarizable in near neutral and low pH aqueous solution [6]. In order to evaluate the polarizability of the specimens under investigation, the anodic polarization plots were replotted after IR correction and presented in Figs. 4.3(a)-(c). The IR correction was implemented by determining the resistance of the electrolytes using the EIS method which is given in a latter section. The results of the anodic polarization measurements are summarized in table 1.

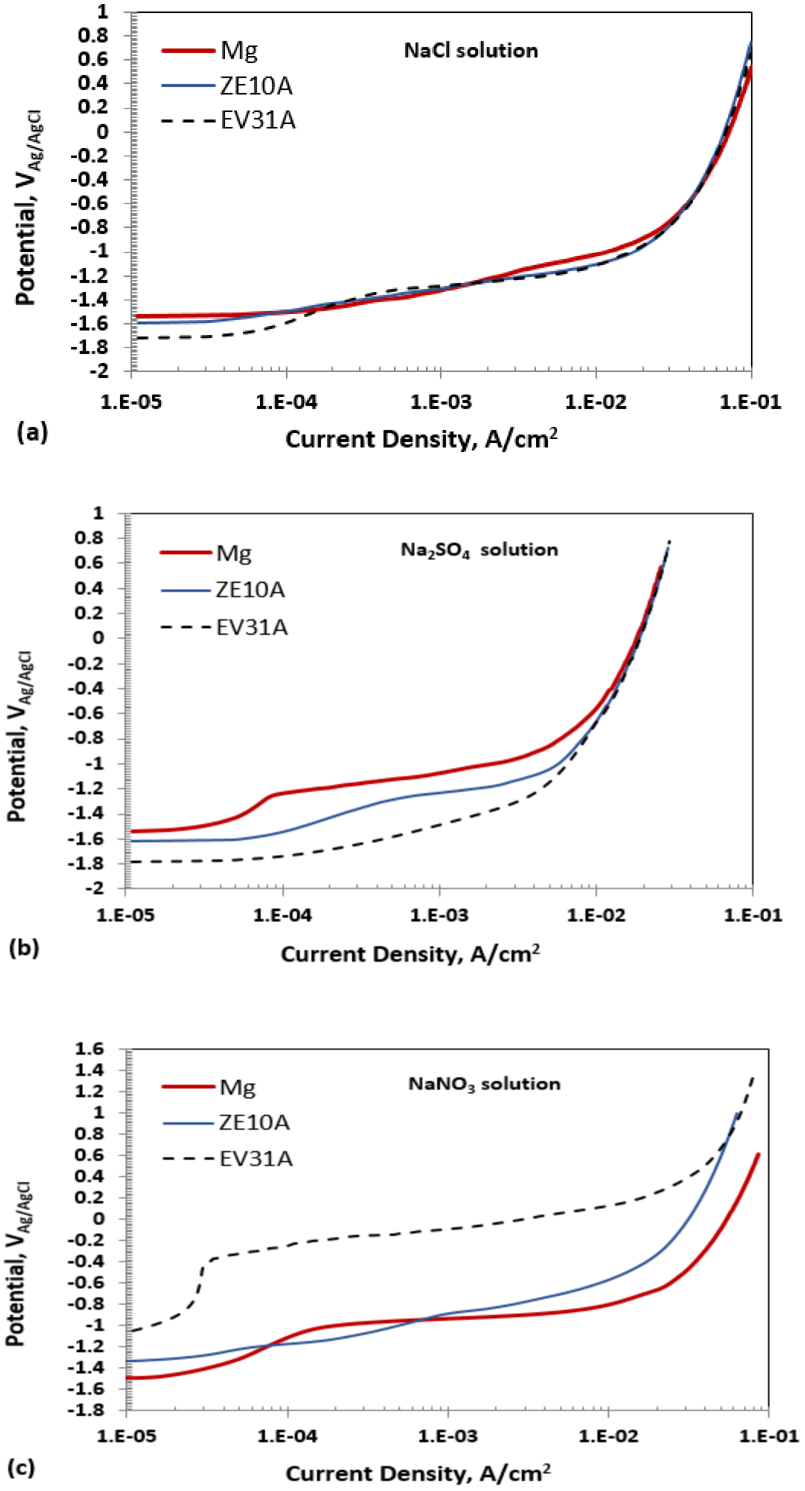

Figure 4.2 Anodic polarization plots of pure Mg, ZE10A, and EV31A specimens in (a) 0.6 M NaCl, (b) 0.1 M Na_2SO_4, and (c) 0.5 M $NaNO_3$ solutions.

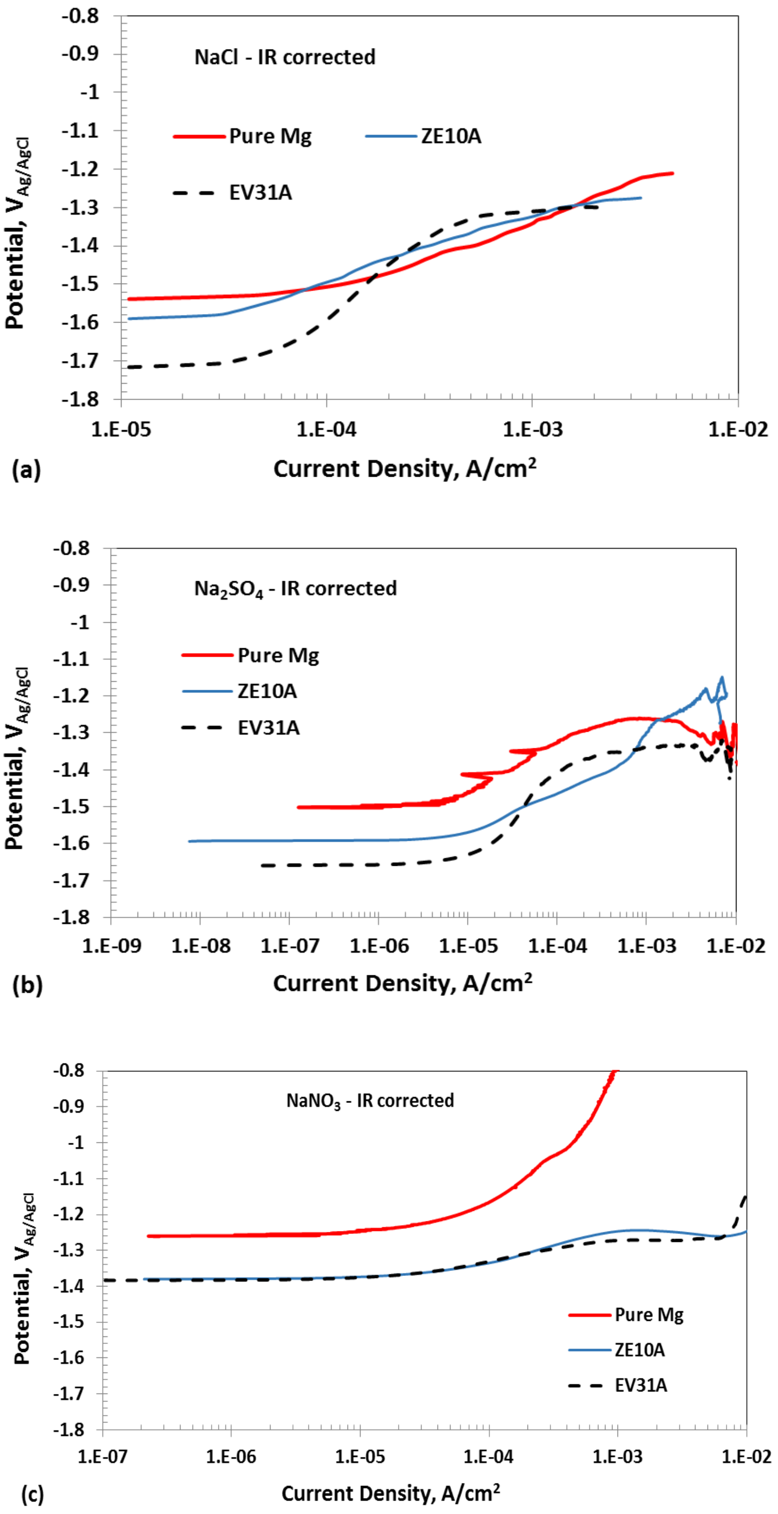

Fig. 4.3 Anodic polarization plots of pure Mg, ZE10A, and EV31A specimens given in Fig. 4.3 after IR corrections in (a) 0.6 M NaCl, (b) 0.1 M Na_2SO_4, and (c) 0.5 M $NaNO_3$ solutions.

Table 4.1 Summary of Anodic Polarization

Sample	**Electrolyte and E_{corr} ($V_{Ag/AgCl}$)**	**Anodic Tafel slope (β_a) (V/decade)**	**Exchange current density for Mg oxidation (A/cm^2)**	**R_p** ***(ohm.cm^2)***	**Calculated average I_{corr} (A/cm^2)**	**Extrapolated I_{corr} (A/cm^2)**
Pure magnesium(Mg)	NaCl (-1.53 V)	0.185 -0.2	1.2 –2.4 x10^{-10}	340- 380	1.0x10^{-4}	3 – 4.8x10^{-5}
	$NaNO_3$ (-1.26 V)	0.27 – 0.3	1.9-3.2 x10^{-10}	190 -212	3.6x10^{-5}	2 - 5x10^{-5}
	Na_2SO_4 (-1.5 V)	0.13 – 0.15	1.4 -2.2 x10^{-12}	504 -530	1.6x10^{-4}	6 - 8x10^{-6}
As received ZE10A(AR)	NaCl (-1.6 V)	.18 – 0.22	1.1 –2.2 x10^{-11}	530-545	1.5x10^{-4}	2 – 4x10^{-5}
	$NaNO_3$ (-1.38 V)	0.1 - 0.11	2x10^{-16}	580 - 610	3.5x10^{-5}	3 - 6.2x10^{-5}
	Na_2SO_4 (-1.6 V)	0.11 – 0.13	1.8 –4.5 x10^{-14}	652 -670	1.0x10^{-4}	0.2 - 1x10^{-5}
ELEKTRON21 (EV31A)	NaCl (-1.7 V)	0.43 – 0.48	6 –8.2 x10^{-7}	338 -347	1.6x10^{-4}	3 - 5x10^{-5}
	$NaNO_3$ (-1.38 V)	0.07 – 0.08	1.0x10^{-19}	554 - 570	6.3x10^{-5}	1.2 -2 x10^{-5}
	Na_2SO_4 (-1.66 V)	0.30 – 0.34	3.2 –6x10^{-8}	392 -404	7.6x10^{-5}	3 -1.5 x10^{-5}

A quick inspection of the anodic polarization plots reveals that the EV31A specimens showed the most active corrosion potentials in all the electrolytes. The corrosion potentials of ZE10A were more active than that of Mg but marginally nobler than that of EV31A except in 0.5M $NaNO_3$ solution. It is well documented that Mg-RE alloys show more negative corrosion potentials [7]. The corrosion potential of Mg was less than -1.5$V_{Ag/AgCl}$ in the NaCl and $NaSO_4$ solutions and -1.26V vs V $_{Ag/AgCl}$ in the 0.5M $NaNO_3$ solution. Song et. A. reported a corrosion potential of -1.62 V_{SCE} in 1N NaCl and -1.545V_{SCE} in 1N Na_2SO_4 solution for 99.96% pure Mg [8]. The relatively noble corrosion potential of the Mg specimens in the current investigation could possibly be attributed to higher impurity contents which is 99.8% purity vs 99.96% purity.

The anodization behaviors of Mg, EV31A and ZE10A appear to be similar in the NaCl solution without IR correction as seen in Figure 4.3(a). However, when IR corrected different degrees of polarizability could be noticed as seen in Figure 4.4(a). The commercial purity Mg specimen was weakly polarizable with a Tafel slope of 0.19 V/decade while EV31A showed polarizability with a Tafel slope of about 0.46 V/ decade as an average. An estimate of exchange current density of Mg/Mg^{2+} redox reaction was carried out by extrapolating the linear portion of the anodic Tafel region back to -2.38V_{SHE}. As summarized in Table 4.1, the exchange current densities for the Mg/ Mg^{2+} oxidation ranged between $1.1x10^{-11}$ and $8.2x10^{-7}$ A/cm^2. The ZE10A specimen showed the lowest value, the EV31A specimen had the largest value and the Mg specimen showed the intermediate value of $2x10^{-10}$A/cm^2.The carrion rates of the specimens are given as I_{corr} values. The i_{corr} values were calculated using the relation [9].

$$I_{corr} = \beta_a . \beta_c / R_p(\beta_a + \beta_c)$$

Where R_p= polarization resistance, β_a and β_c are anodic and cathodic Tafel slopes.

The i_{corr} values were determined graphically by linear extrapolation of the IR corrected anodic and cathodic polarization plots to the E_{corr} values. The i_{corr} values are summarized in Table 1. The calculated and extrapolated values match with each other in the Na_2SO_4 and $NaNO_3$. Solutions well but not in the NaCl solution. The reason for this mismatch is not known but could be associated with highly localized reactivity of the chloride ions, where partially covered surface films were reported [10]. The extrapolated I_{corr} values of the specimens in 0.6M NaCl solution indicated that all three materials showed a similar corrosion kinetics. The corrosion current was in the range of 13-50 µA/ cm^2. Feng et. Al reported an i_{corr} value of 59.3+-1.5 µA/ cm^{2}for pure Mg in 3.5wt% NaCl solution. The calculated i_{corr} value of Mg in NaCl solution was a bout 100NA/cm^2 which is twice the extrapolated value. Handy and Butt [11] reported the values i_{corr}=73µA/cm^2 and Rp=350 Ω for EV31A-T6 in 3.5wt% NaCl which is closely match with the reported value in the investigation. The anodic polarization behaviors in the 0.1M Na_2SO_4 solution showed a similar trend as the observed in the 0.6m NaCl solution as seen in Fig.4.3 (b) and 4.4(b). The Mg and ZE10A specimens were weakly polarized with a Tafel slope in the range of 0.11-0.15V/decade whereas EV31 specimen showed a Tafel slope of about 0.32 V/ decade. The exchange current densities for Mg/Mg^{2+} oxidation was lower and the Rp values were higher than that observed in the NaCl solution. The i_{corr} values was 6-8 µA/cm^2 for Mg, 2-10 µA/cm^2 for ZE10A and 3-15µA/cm^2 for EV31A. Ardelean et al [12] investigated the corrosion behavior of pure Mg and Mg-RE alloy WE43 in 0.5M Na_2SO_4 solution and reported much lower values of Rp (26.6 and 128 ohm.cm^2 for MG and WE43 respectively) and higher i_{corr} values (581 and 6442 µA/cm^2 for Mg and WE43 respectively) than what observed in this study. However, the concentration of Na_2SO_4 was lower (0.1M vs 0.5M) in this study.

More noble corrosion potentials were recorded in the 0.5M $NaNO_3$ solutions. A similar result was reported was reported by Richey et al [13]. A weak polarizability was observed for the ZE10A and EV31A specimens with an anodic Tafel slope around V/decade. The EV31A specimen had the highest R_p value in the $NaNO_3$ solution. The I_{corr} values of all the specimens were in the range of 12-62µA/cm^2. Overall, when the anodic polarization behaviors of the three materials were compared for application as anode materials, it was observed that 0.5M $NaNO_3$ could be a potential electrolyte that could result in weak polarizability and low self-discharge. However, nobler corrosion potentials could result in self-discharge potential. The EV31A alloy shows more active corrosion potentials in all the electrolytes which could be advantageous for exhibiting high discharge potentials but revealed relatively higher polarizability than other two materials. Since the anodic polarization behavior could not distinguish the superior material for Mg-air battery anode application, the cathodic behaviors, especially the negative differential effect (NDE) of the materials need to be considered.

Figs 4.4(a)-(c) show the cathodic polarization behaviors of the Mg, ZE10A and EV31A specimens in 0.6M NaCl, 0.1M Na_2SO_4 and $NaNO_3$ solutions without IR correction respectively. Three materials showed similar cathodic polarization in the NaCl and Na_2SO_4 solutions whereas noticeable difference was recorded in the $NaNO_3$ solution. The nonlinear concentration polarization type behavior could be attributed to the IR drop and the resistance due to significant hydrogen evolution on the surface of the specimens. Similar kind of cathodic polarization plots were reported for MG-Sn and Mg-Sb alloys in 0.1M NaCl solution [[18]]. It is difficult to derive Tafel slope from these nonlinear polarization behaviors. Therefore, IR-corrected plots are presented in Fig 4. 5(a)-(c) which facilitate a clear delineation of the cathodic polarization behavior of different materials.

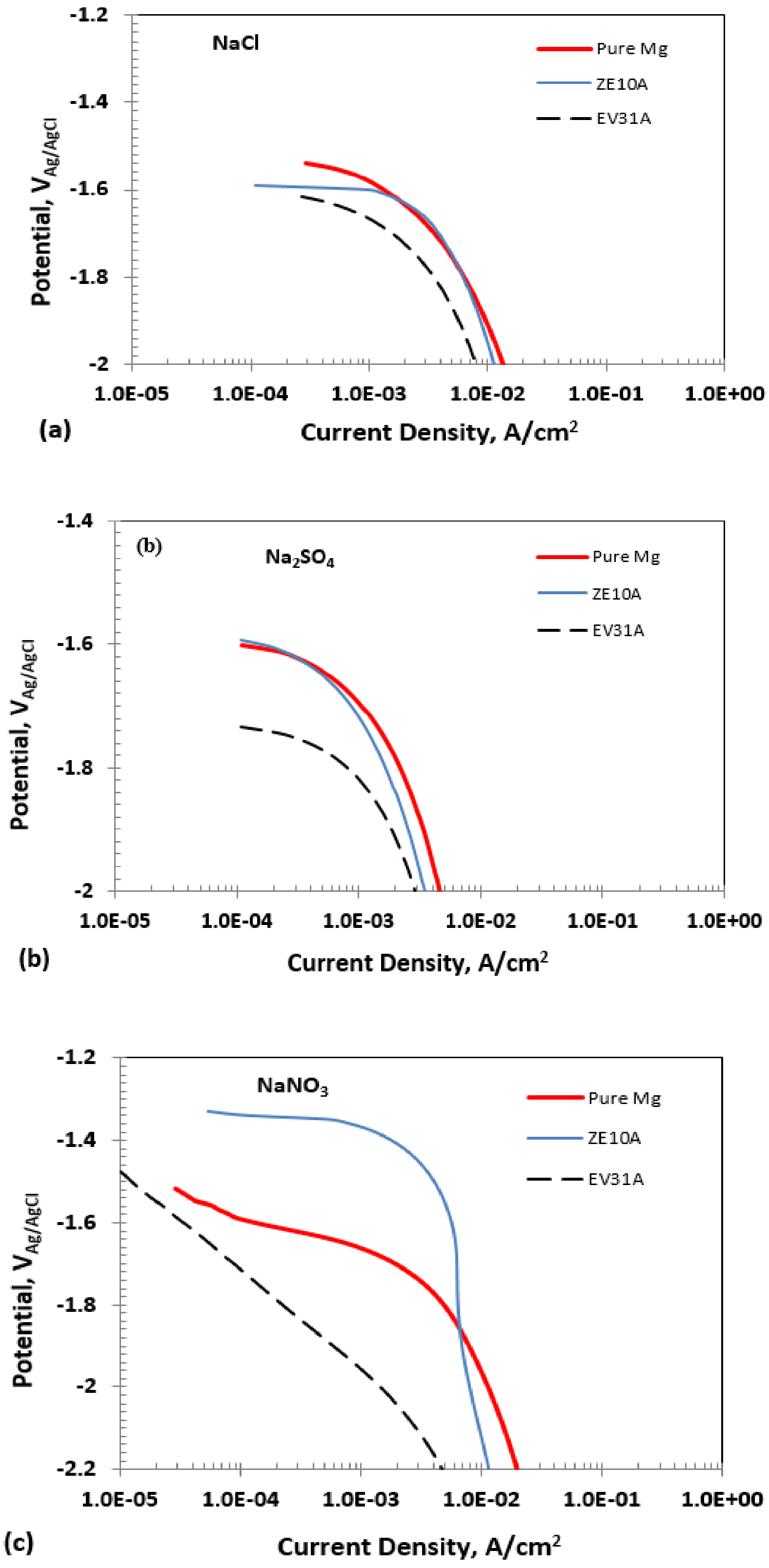

Figure 4.4 Cathodic polarization plots of pure Mg, ZE10A, and EV31A specimens in (a) 0.6 M NaCl, (b) 0.1 M Na_2SO_4, and (c) 0.5 M $NaNO_3$ solutions.

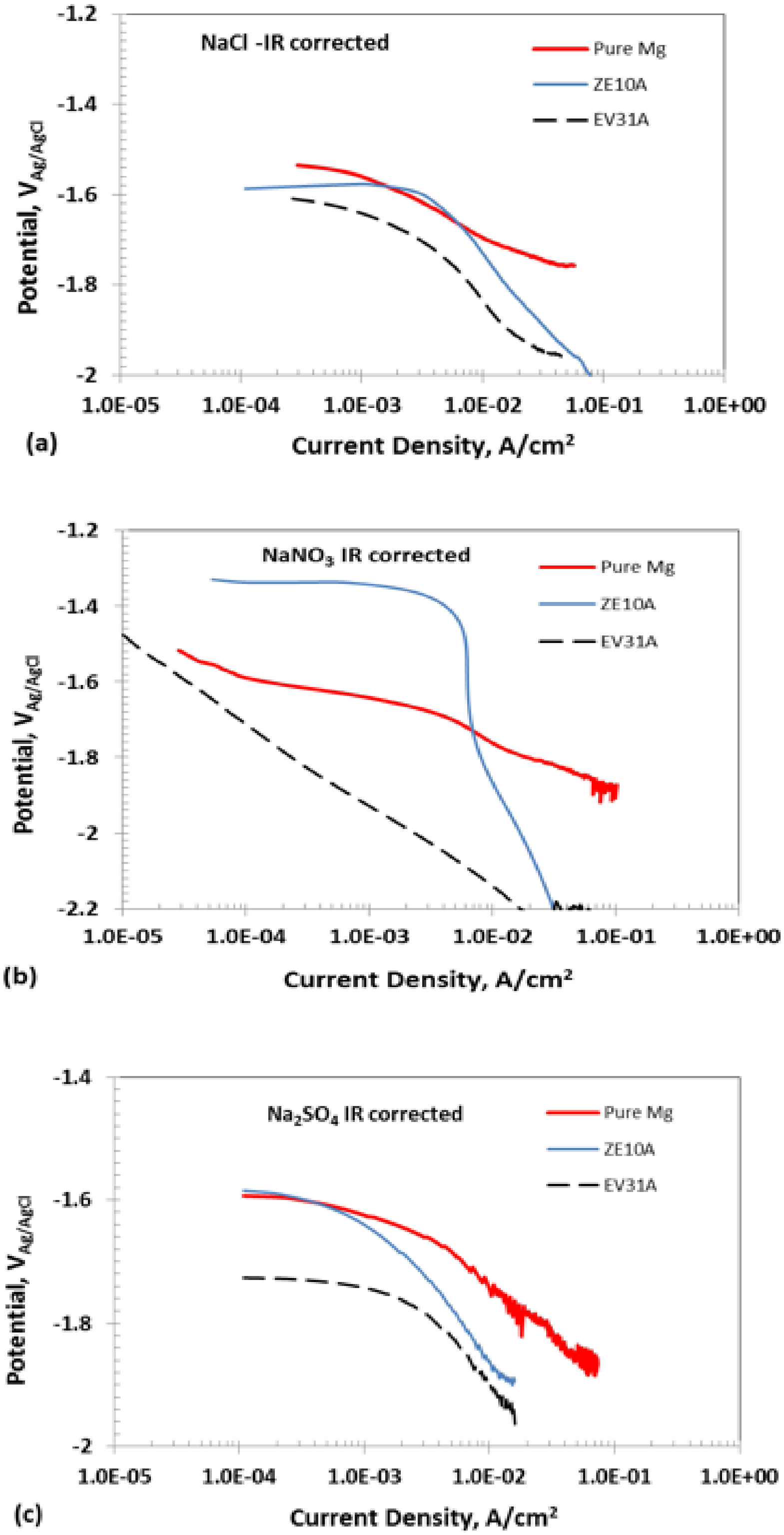

Figure 4.5 Cathodic polarization plots of pure Mg, ZE10A, and EV31A specimens given in Fig. 4.4 after IR corrections in (a) 0.6 M NaCl, (b) 0.1 M Na_2SO_4, and (c) 0.5 M $NaNO_3$ solutions.

Table4.2 Summary of Cathodic Polarization

Sample	**Solution**	**HER Over-potential, V at -10 mA/cm^2**	**Cathodic Tafel slope (β_c) (V/decade)**	***Exchange current density for H_2*** **(A/cm^2)**
Pure magnesium(Mg)	NaCl	1.05 -1.1	-0.160 to -0.172	3 x10^{-9} - 2x10^{-8}
	NaNO$_3$	1.13 – 1.17	-0.05 to -0.08	9x10^{-13} – 1.5 x10^{-11}
	Na$_2$SO$_4$	1.12 – 1.14	-0.15 to -0.17	8 x10^{-10} - 5.2x10^{-8}
As received ZE10A(AR)	NaCl	1.115 -1.13	-0.32 to -0.36	1.2x10^{-7} – 4.6x10^{-6}
	NaNO$_3$	1.2 -1.3	-0.18 to -0.22	5.3 x10^{-9} - 2.9x10^{-8}
	Na$_2$SO$_4$	1.22 – 1.28	-0.23 to -0.28	2.4x10^{-8} – 1 x 10^{-7}
ELEKTRON21 (EV31A)	NaCl	1.2 – 1.26	-0.3 to - 0.33	4.0x10^{-8} – 1.2 x 10^{-6}
	NaNO$_3$	1.5 – 1.58	-0.21 to -0.24	1.23 x10^{-9} - 1.9x10^{-9}
	Na$_2$SO$_4$	1.28 – 1.32	-0.24 to -0.26	1x10^{-8} – 6.9 x10^{-8}

The Tafel slopes of cathodic polarization of the specimens in NaCl solution varied from -0.16V to -0.36V/decade. The ZE10A specimen showed a relatively higher Tafel slope in the rage of -0.32V to -0.36V/ dec, than other two materials. A Tafel slope in the range of -0.16V to 0.172V/dec was recorded for the pure Mg specimen in the 0.6M NaCl solution. Frankel et al [19] reported a Tafel slope of -0.26V/decade for the pure Mg in 0.1M NaCl. El-Taib Heakal et al [20] reported a cathodic Tafel slope -0.18V/dec for the pure Mg and AZ91D alloy, the MG-RE alloys, ZE10A and EV31A showed a higher cathodic Tafel slope as seen in Table 2. The cathodic reaction occurring on the MG and MG alloy specimens is considered to be water reduction and hydrogen evolution ($2H_2O+2e^- \longrightarrow H_2+2OH^-$) [21].

Therefore, the over potentials required for hydrogen evolution at a current density of -10mA/cm^2 on three specimens are summarized in the Table 2. It is noted that the EV31A specimen required a higher over potential (1.2-1.26V) than the other two specimens in NaCl solution. There was no significant difference in the overpotential values between the ZE10A and pure Mg specimens. The exchange current densities for the redox reaction in NaCl solution on the Mg and Mg-RE alloys varied widely from $3x10^{-9}$ and $4.6x10^{-6}A/cm^2$. Pure Mg specimens showed the exchange current density at the lower end of the spectrum ($3x10^{-9}A/cm^2$) and the ZE10A specimen showed at the higher end of the spectrum ($4.6x10^{-6}$ A/cm^2). Among the three electrolytes investigated, the $NaNO_3$ solution showed the lowest cathodic Tafel slopes and lowest exchange current densities, indicating that NDE could be less in this solution. The pure Mg specimen showed the lease Tafel slope in the 0.5M $NaNO_3$ solution and the EV31A showed the highest Tafel slope. Similar trend was observed in the 0.1M Na_2SO_4 solution. The exchange current densities in the Na_2SO_4 solution for the hydrogen evolution reaction were higher than those observed in the $NaNO_3$ solution but lower in the NaCl solution. These cathodic polarization results indicated that the NDE will be lower in the EV31A specimen than other two materials and lower in the $NaNO_3$ solution than other two electrolytes.

The obtained exchange densities (i_o, H_2) for hydrogen evolution were lower than the reported values in the literature. For example, Frankel et al [19] derived the i_o,H_2 values to be $4x10^{-5}$, $8x10^{-4}$ and $10mA/cm^2$ respectively. These reported high exchange current densities for hydrogen reduction cannot be directly compared with the values obtained during the cathodic polarization. The cathodic polarization in this investigation was carried out on the freshly polished specimens. The catalytic activity of this surface would be different from that of the actively corroding surface, as noted by other researchers [22].

Figure4.6(a)-(c) show the EIS results as Bode plots of the pure MG, ZE10A and EV31A specimens in three different electrolytes. The EIS was carried out before the discharge experiments. The impedance data were fitted with equivalent electrical circuits (EEC) to understand the electrochemical processes occurring at the freely corroding condition without any polarization. The EEC fitted data are summarized in the supporting information as Tables S1-S3The EEC varied depending on the material and the electrolyte.

The impedance data of the pure Mg specimen in 0.6M NaCl solution showed a single time constant and decreasing impedance at low frequencies. Therefore, the data could be fitted with an EEC of a single loop RC circuit consisting of additional inductor and resistor connected in series as shown in Table S1(a). Similar type of EEC was proposed for Mg-9Al-Zn anodes in 3.5wt% NaCl solution by Li et.al [8]. In this circuit R_s represents the electrolyte resistance, Q represents the interfacial capacitance with distributed time constants due to surface roughness of the electrode [39]. R_2 represents the charge transfer resistance and R_1 and L_1 are associated with the surface adsorption of intermediate corrosion products.

The physical significance of an inductor in an electrochemical process has been discussed by Harrington and Van den Driessche [23]. These authors showed that at least two electro transfer steps are required for the inductive behavior with electron transfer occurring on both the adsorbate and free sites on which adsorption takes place. Since the EIS was carried out at OCP, the inductive behavior could be associated with anodic or cathodic (hydrogen evolution) reactions. The impedance behavior of the pure Mg in 0.1M Na_2SO_4 showed two-time constants and the EIS data could be fitted with an EEC with 2-RC loops connected in series as shown in Table S1(b). A similar EEC was proposed by Baril and Pebere [24]. In this EEC, Q_1 and Q_2 are leaky capacitors associated with interfacial capacitance and space charge layer of the surface layer formed on the specimen respectively. The reported double layer capacitance of 9μfarad/cm^2 under similar experimental condition is of the same order of magnitude of the Q_1 value in this study [25]. R_1 and R_2 are associated with the charge transfer resistance across the electrode/ electrolyte interface and the film resistance respectively. At very low frequencies the value of R_1+R_2 could be related to the polarization resistance (R_p). As noted, this value is much lighter than that determined by the linear polarization (L_p) method. The R_p value obtained through the Lp method closely matches with the value of R_1.

The EEC for the EIS behavior of pure Mg in 0.5M $NaNO_3$ is given in Table S1(c). A similar equivalent circuit in 3.5wt% NaCl solution. The loop consisting of the components Q_1, R_1, L_1 and R_2 are associated with electrode/ electrolyte interface and the loop consisting of Q_2 and R_3 is associated with the formation of a surface layer on the electrode. At very low frequencies, the Q_1 and Q_2 will have very large impedance and the impedance due to L_1 will be significantly low. Therefore, the polarization resistance (f=0) of the system will be given by the relation: $R_p=R_3+R_1R_2/R_1R_2$ which is 5135 Ω. The inductance value in the $NaNO_3$ solution is much lower than that observed in the NaCl solution. If the absorption process is associated with the hydrogen evolution reaction, then the lower value observed in the nitrate solution indicated lower NDE than that observed in the NaCl solution. The magnitude of the Q_2 which is related to the space charge layer capacitance of the surface layer is similar to the Q_2 observed in the Na_2SO_4 solution.

The impedance behavior so EV31A in the NaCl and Na_2SO_4 solutions could be fitted with one EEC as given the Table S2(a). King et al [27] reported this type of EEC for the corrosion of pure Mg in NaCl solutions. In this EEC, the electrode/ electrolyte interface and the surface layer are not separated as individual R-C loops. Instead of having two separate RC loops and connecting them in series, the entire electrochemical system is represented as a porous film model with adsorption. The current components represent the usual processes described in the previous EECs. Here the polarization resistance at zero frequency (R_p) is given by the relation $R_p=R_1(R_2+R_3)/R_1+R_2+R_3$ [27]. The R_p values of EV31A in NaCl and Na_2SO_4 solutions could be calculated from the EIS results and given as 537 and 599 Ω, respectively. Interestingly, the R_p values determined from the EIS data and the linear polarization (L_p) data as given in Table 1, closely match with each other. The EIS data of the EV31A specimen in the 0.5M $NaNO_3$ solution was fitted with a different equivalent circuit as shown in Table S2(b). The corrosion of EV31A in $NaNO_3$ was observed to be diffusion controlled with a Warburg coefficient (in the unit of admittance) of $2.434x10^{-3}S. s^{0.5}$. The charge transfer resistance was 661 Ω and the leaky capacitance due to electrolyte interface and a surface layer was an order of magnitude higher than the values noted for pure Mg.

The EIS data of ZE10A specimens in all three electrolytes could be fitted well with a single EEC as seen in Table S3. From the EIS data, the R_p values could be calculated as 340,740 and 400Ω in NaCl, Na_2SO_4 and $NaNO_3$ solutions respectively. The comparison of the EIS results of both the EV31A and ZE10A specimens in the NaCl and Na_2SO_4 electrolytes indicate the contradicting corrosion resistance behavior between these two solutions. The ZE10A showed lower corrosion resistance in the NaCl solution and higher corrosion resistance in the Na_2SO_4 solution than that of EV31A. The R_p values obtained from the EIS results of those two materials do not agree ell with the R_p values of LP method.

Figure 4.7 (a)-(c) show the EIS results as Bode plots during galvanostatic discharge at $10mA/cm^2$ after reaching a steady state potential condition. The EIS data of the pure Mg specimens in all three solutions could be fitted well with a single EEC as shown in Table S4 (supporting info). Since, the EEC of the galvanostatic discharge was different from that modeled at the OCP in the magnitude of the current components cannot be directly compared.

However, the R_p values can be compared. The galvanostatic EIS also included an adsorption component indicating the NDE effect (hydrogen adsorption and desorption). The adsorption value in terms of inductance was the highest in the $NaNO_3$ solution. It should be noted that the hydrogen evolution rate was lower in this solution than in the other two solutions. Therefore, the high inductance value could be associated with possible high binding energy of the surface sites to H_{ads} in the $NaNO_3$ solution. The Q_1 and Q_2 values that are related to interfacial capacitance and space charge layer capacitance respectively are lower in the $NaNO_3$ than the values noted in the NaCl solution. The R_p values during galvanostatic discharge calculated at the zero frequency of the EIS data are 13,226 and 232 Ω in NaCl, na_2SO_4 and $NaNO_3$ solutions respectively. The low R_p value in NaCl solution indicates that the discharge activity is higher in this solution. The EIS data of the EV31A specimens showed a predominantly a single time constant in the NaCl and Na_2SO_4 solutions and two-time constants in the $NaNO_3$ solution. Because of a minor change in the slope of the Bode plots at very low frequencies, the EIS data could be fitted well with EECs having a single time constant and two-time constant as well as illustrated in Table S5(a) and S5(b). At open circuit condition a two-time constant behavior was observed. Therefore, comparison of the two tie constant data given in Table S5(b) and S(2) will help understand the discharge process occurring on the EV31A specimens. During the galvanostatic discharge the resistance associated with the adsorption (R_1) decreased significantly, the inductance increased and the interfacial capacitance (Q_1) increased as compared to the OCP condition in general. The space charge layer capacitance (Q_2) also increased under the galvanostatic discharge. However, the resistance associated with the surface layer (R_3) did not change significantly in the NaCl solution but decreased significantly in the Na_2SO_4 solution. The R_p values (at zero frequency) calculated from the EIS data are 55, 134 and 43 Ω in the NaCl, Na_2SO_4 and $NaNO_3$ solutions respectively. The values are in order of magnitude lower than that observed in the OCP condition. The R_p values calculated using a single time constant EEC are 72 and 192 Ω in the NaCl and Na_2SO_4 solutions.

The EIS data of the ZE10A during the galvanostatic discharge are fitted with the same EEC that is used in the OCP condition. The values are summarized in Table S6. These values could be compared with eh EIS data of OCP given in Table S3. The values of R_1, R_2 and R_3 decreased drastically during the galvanostatic process. Interestingly the inductance values showed a different trend from those observed for the other two materials. The inductance decreased in the NaCl and $NaNO_3$ solution upon galvanostatic conditioning as compared to that observed int eh OCP conditioning. The capacitance due to space charge layer increased in the NaCl and $NaNo_3$ solutions. The interfacial capacitance increased upon galvanostatic discharging only in the NaCl solution and decreased significantly while galvanostatic discharging to the values of 13,115 and 84 Ω in NaCl, Na_2SO_4 and $NaNO_3$ solutions respectively.

Overall, the EIS results indicate that the NaCl solution showed the highest activity for anode discharge followed by $NaNO_3$ and $NaSO_4$. The pure Mg showed the highest discharge activity in the NaCl solution. However, the R_p values of Mg are higher in the Na_2SO_4 and $NaNO_3$ solutions than other two materials. ZE10A showed lower R_p values in the NaCl and $NaNO_3$ solution than EV31A did.

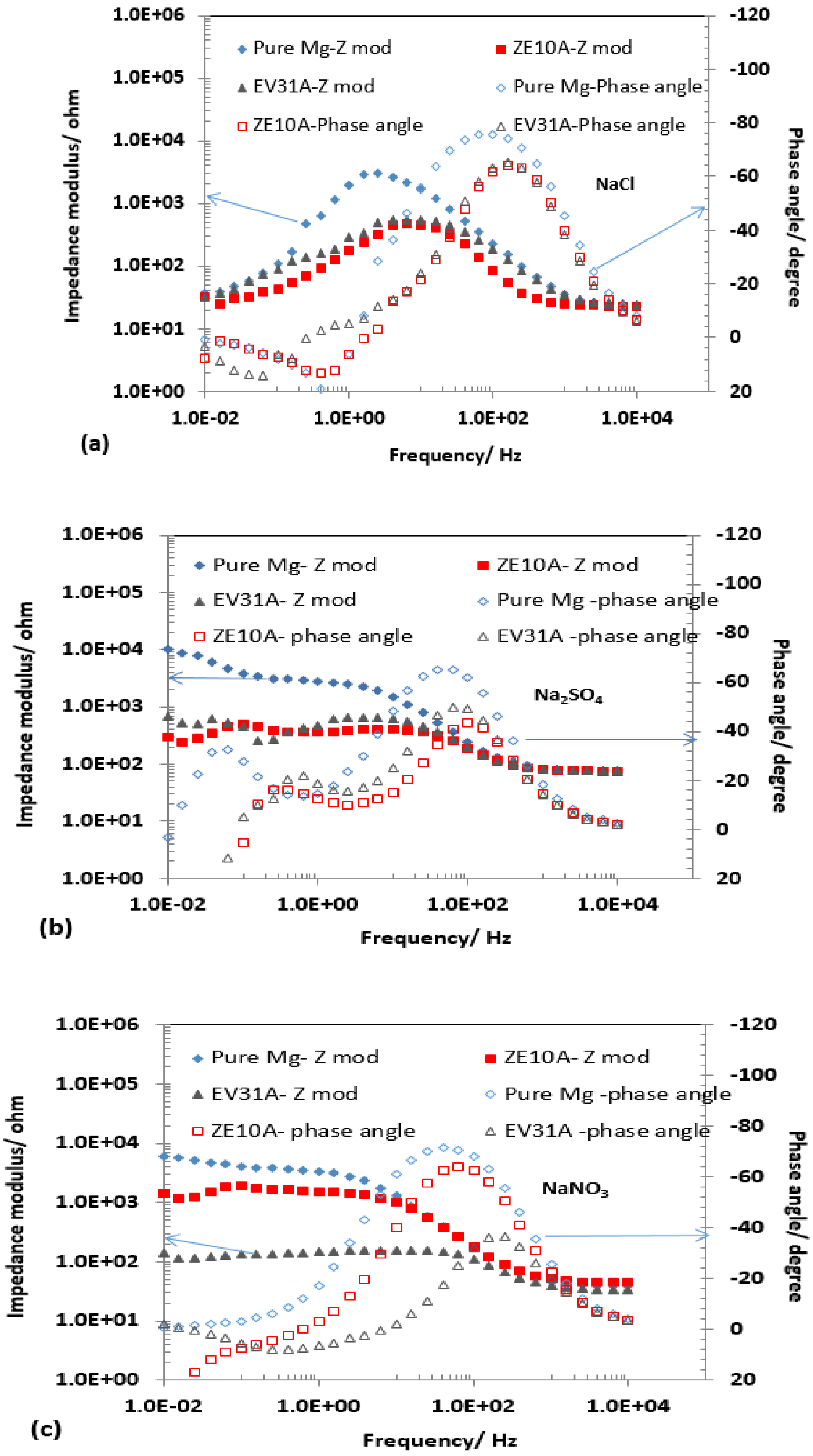

Figure4.6 Bode plots of Mg, ZE10A and EV31A before discharge in solutions: (a) NaCl, (b) Na$_2$SO$_4$ and (c) NaNO$_3$

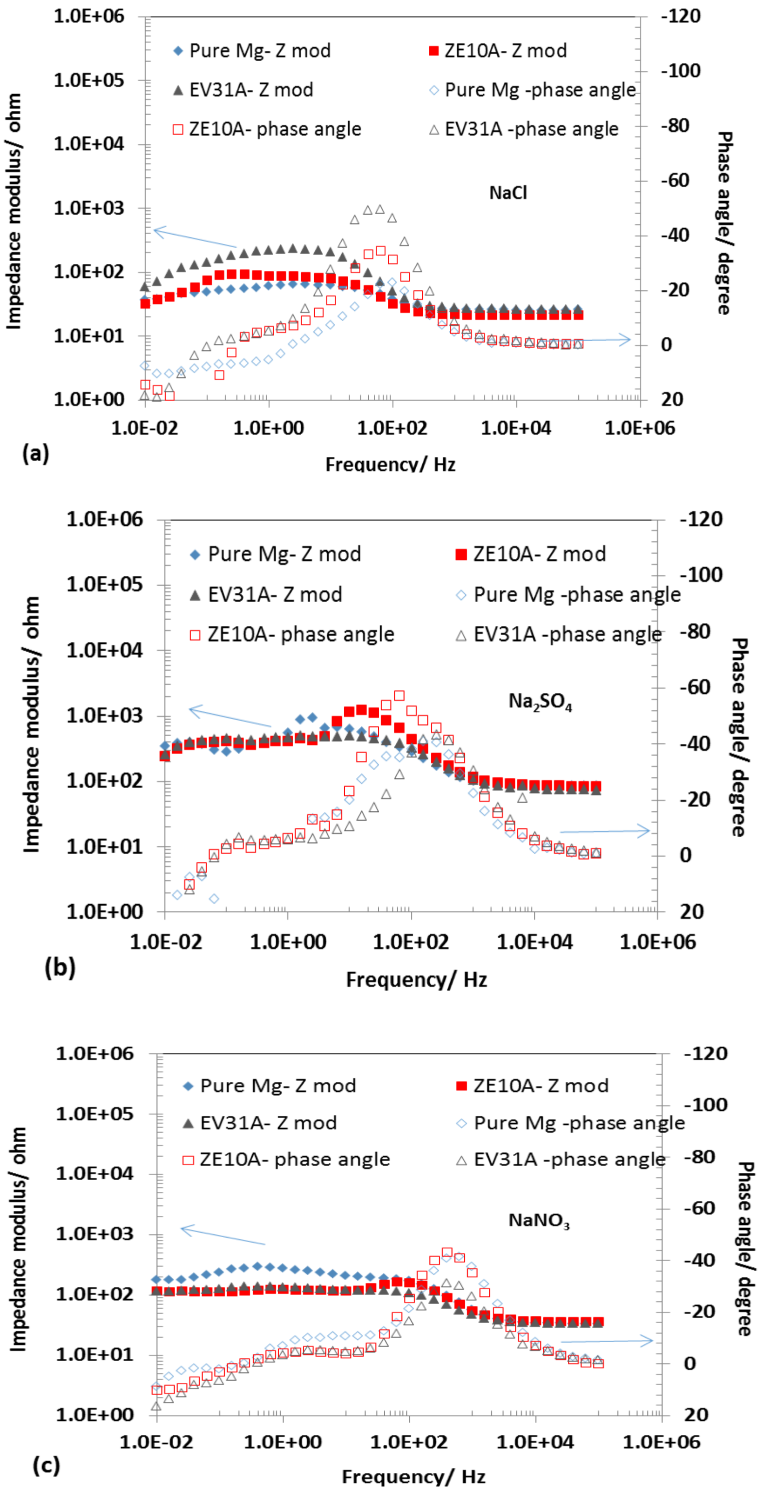

Figure 4.7 Bode plots of pure Mg, ZE10A, and EV31A specimens after galvanostatic discharge at 10 mA/cm^2 in (a) 0.6 M NaCl, (b) 0.1 M Na_2SO_4, and (c) 0.5 M $NaNO_3$ solutions.

4.3 Measurement of HER and Analysis of NDE

Table 4.3 summarizes the hydrogen evolution rate (ml/cm^2.h) during potentiostatic conditioning of the three materials in the three electrolytes. Increasing the potentials in the anodic direction increases the hydrogen evolution rate for all the materials in all three solutions. The hydrogen evolution rate could not be measured at low anodic potentials in the $NaNO_3$ solution mainly because of the low hydrogen evolution rate in the nitrate electrolyte and the experimental time was not sufficiently long to record a reproducible value. All the materials showed significant hydrogen evolution rate in the NaCl solution. An evolution rate of 1ml/cm^2.h of hydrogen corresponds to 2.39mA/cm^2 current density. At -1.5 $V_{Ag/AgCl}$, all three materials showed a similar hydrogen evolution rate of about 0.6ml/cm^2.h. The Mg-RE alloys showed relatively higher hydrogen evolution rate than the pure Mg specimen indicating that the NDE activity was higher for the Mg-RE alloys in the NaCl solution. Similar trend was observed in other two electrolytes. It should be noted that the potentials were not IR corrected. The recorded hydrogen evolution rate at -1.1 $V_{Ag/AgCl}$ for the 99.98% pure Mg in 0.6M NaCl was almost twice the value reported for 99.99% pure Mg in 0.1M NaCl [22]. The higher hydrogen evolution rate could be attributed to high impurity content that had more catalytic activity for hydrogen. The hydrogen evolution rates were measured during the galvanostatic conditions and presented in Table 4.4. Pure magnesium showed the lowest hydrogen evolution rates in the $NaNO_3$ solution followed by the Na_2SO_4 solution. The hydrogen evolution rate measured for pure Mg in 0.6M NaCl at 1mA/cm^2 was 0.26ml/cm^{2}hwas comparable to 0.85ml/cm^2 in 4 hour at 1mA/cm^2 for high purity Mg in 0.1 M NaCl by Frankel et.al [23]. These authors reported 0.76ml/cm^2 in 24 min at 10mA/cm^2 which was 68% of the value of this investigation under similar conditions. Thomas et.al [24] reported much higher hydrogen evolution rates on pure

Mg in 1 M NaCl solution as compared to AZ91 alloy. The values at 1mA/cm^2 were 1.44 and 0.6ml/cm^2.h for pure Mg and AZ91 respectively.

Table 4.3 Hydrogen Evolution Rate(ml/cm^2.h) at Different Potentials

Sample	**Solution**	**-1.5V**	**-1.3V**	**-1.1V**	**-0.9V**	**-0.7V**	**-0.55V**
Pure Mg	NaCl	1.438672	8.6148	11.19924	14.38672	20.07248	23.00152
	$NaNO_3$	0	0	0	0	1.438672	2.868728
	Na_2SO_4	0	0	0	2.868728	4.3074	5.746072
ZE10A (AR)	NaCl	1.438672	18.09108	22.91537	25.8444	30.1518	34.4592
	$NaNO_3$	0	0	0	4.3074	5.746072	7.176128
	Na_2SO_4	0	1.438672	2.868728	4.3074	5.746072	8.6148
EV31A(AR)	NaCl	1.438672	8.6148	15.50664	18.09108	25.8444	28.42884
	$NaNO_3$	0	0	0	1.438672	2.842884	4.3074
	Na_2SO_4	0	1.438672	2.58444	3.161632	5.453168	8.6148

Table 4.4 Rate of Hydrogen Collection (ml/cm^2 per hour) on Mg, ZE10A and EV31A in 0.6M NaCl, 0.5M $NaNO_3$ and 0.1M Na_2SO_4 at Positive Current Rates

		Hydrogen evolution rate (ml/cm^2.h) at galvanostatic conditioning			
Sample	**Solution**	**1mA**	**10mA**	**20mA**	**100mA**
Pure magnesium (Mg)	NaCl	0.267	3.25	6.12	11.59
	$NaNO_3$	0.127	0.277	0.511	3.0
	Na_2SO_4	0.17	1.45	3.1	18.9
As received ZE10A(AR)	NaCl	0.16	1.8	3.8	19.2
	$NaNO_3$	0.12	0.4	0.67	10.2
	Na_2SO_4	0.15	1.54	3.37	19.4
ELEKTRON21 (EV31A)	NaCl	0.18	1.9	4.1	21.6
	$NaNO_3$	0.14	0.66	0.96	12.0
	Na_2SO_4	0.23	2.1	4.1	19.5

4.4 Analysis of Discharge Behavior of Anodes

Application of current instantaneously increase the potential to more noble values and the potential decayed to lower values. In case of the EV31A specimen that showed the more active corrosion potential, the potential increased to about -0.876V from -1.64 $V_{Ag/AgCl}$ for the first 10s of the current application and then decayed relatively faster than the rate observed for ZE10A and reached a plateau value of -1.52V $_{Ag/AgCl}$ after about 50s of current impression. A steady state potential was reached only after about 160s in case of the ZE10A specimen. All the three materials showed about same discharge potential in the NaCl solution under different galvanostatic conditions as seen in figure 4.8 (a)-(c). The discharge potentials were -1.56V, -1.29V and -1.08V $_{Ag/AgCl}$ at the current densities of 1, 10 and 20 mA/cm^2 respectively. The

ZE10A specimen showed marginally more noble discharge potential than the other two materials. It should be noted that higher the discharge potential, lower will be the cell potential of the Mg-air battery. The reported potentials are not IR corrected. In fact, in real life battery the potentials include the IR component and the potential loss due to IR would be dissipated as heat and increase the battery temperature.

Figures 4.9(a)-(c), show the chronopotentiometry results for 1, 10 and 20mA/cm^2 current densities in 0.1M Na_2SO_4 respectively. Strong potential pulses were observed at 1mA/cm^2 and with the increase in the current density the height of potential pulse was significantly low. The potential depth for the pure Mg was higher compared to the other two alloys. The potential decay rate was slower for the EV31A than that observed for the ZE10A. After about 300s, all three materials showed almost a similar discharge potential of -1.45 $V_{Ag/AgCl}$. At higher current densities, the discharge potentials differed significantly between the different materials. Pure Mg specimen showed the lowest discharge potential of -0.98V $_{Ag/AgCl}$ that slowly decreased with time, while a plateau potential of 0.64 $V_{Ag/AgCl}$ was noted for EV31A and the potential of ZE10A showed an increasing trend with time around a value of -0.4V at 10mA/cm^2. When the applied current density was 20mA/cm^2, the pure Mg and ZE10A specimens showed almost a similar discharge potential around -0.56$V_{Ag/AgCl}$, whereas the EV31A had a potential of 0.21$V_{ag/agcl}$. The very high potential could be attributed to a high IR drop due to bubble formed during hydrogen evolution and a thicker corrosion product formed on the surface.

Figures 4.10(a)-(c) show the chrono potentiometric results for 1, 10 and 20 mA/cm^2 in the $NaNO_3$ solution respectively. It is interesting to note that, unlike in the other two electrolytes, the three materials showed different discharge potentials for a given current density. The EV31A specimens showed the lowest discharge potentials in all the current densities and pure Mg specimens showed the highest discharge potentials. This observation indicated that the Mg-RE alloys had better discharge characteristics as anode for Mg-air battery.

The discharge potentials at 1mA/cm^2 in 0.5M $NaNO_3$ solution for the EV31A, ZE10A and Pure Mg were -1.35V, -1.25Vand -1.17$V_{Ag/AgCl}$, respectively. Increasing the current density to 10mA/cm^2 increased the discharge potentials to -0.96V, -0.91V and -0.56$V_{Ag/AgCl}$ for the EV31A, ZE10A and pure Mg respectively. The EV31A material showed slower potential decay behavior in the $NaNO_3$ solution, like the one observed for the Na_2SO_4 solution.

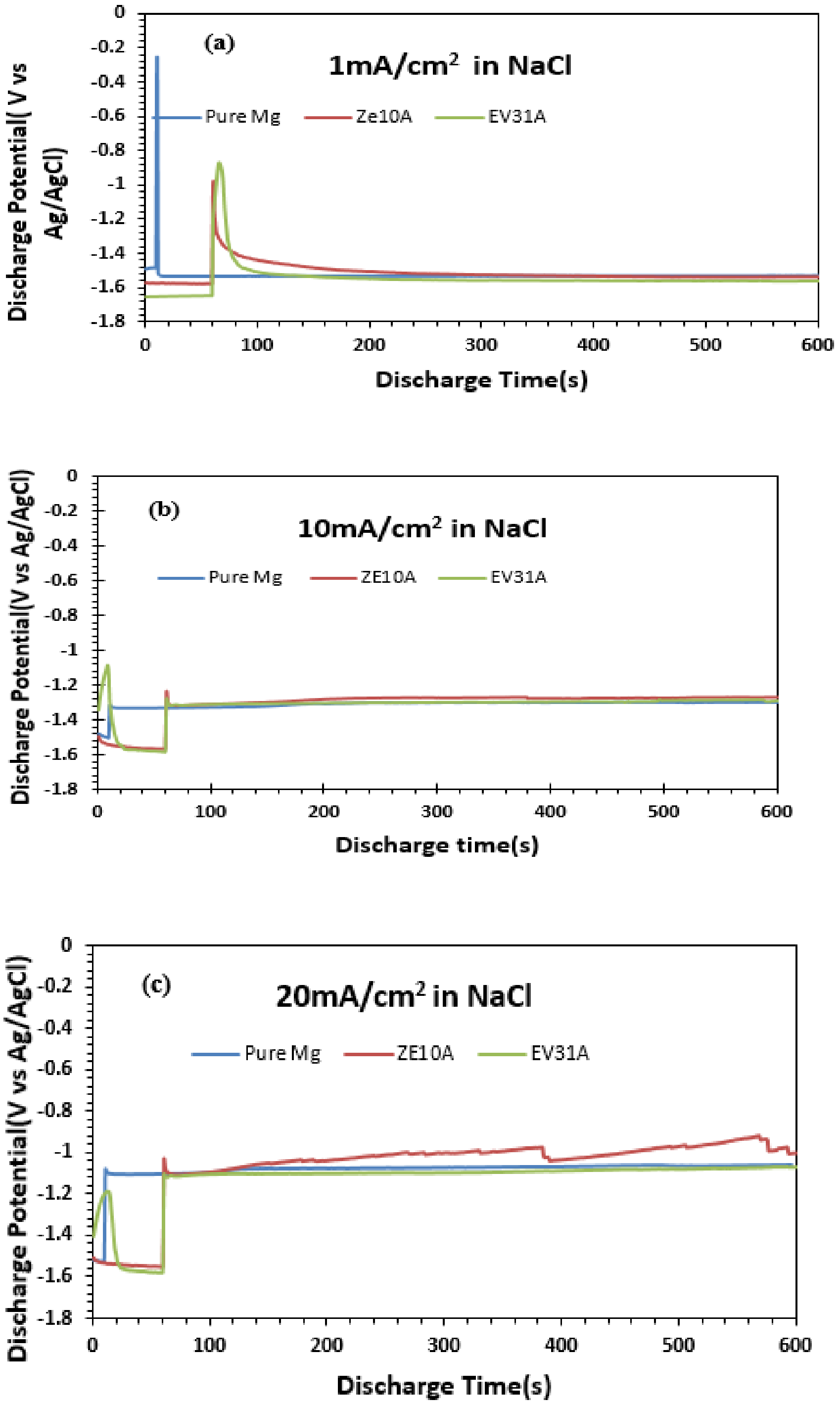

Figure 4.8 Discharge Behavior of Pure Mg, ZE10A and EV31A in 0.6M NaCl at (a)1ma/cm^2, (b) 10mA/cm^2 and (c) 20mA/cm^2

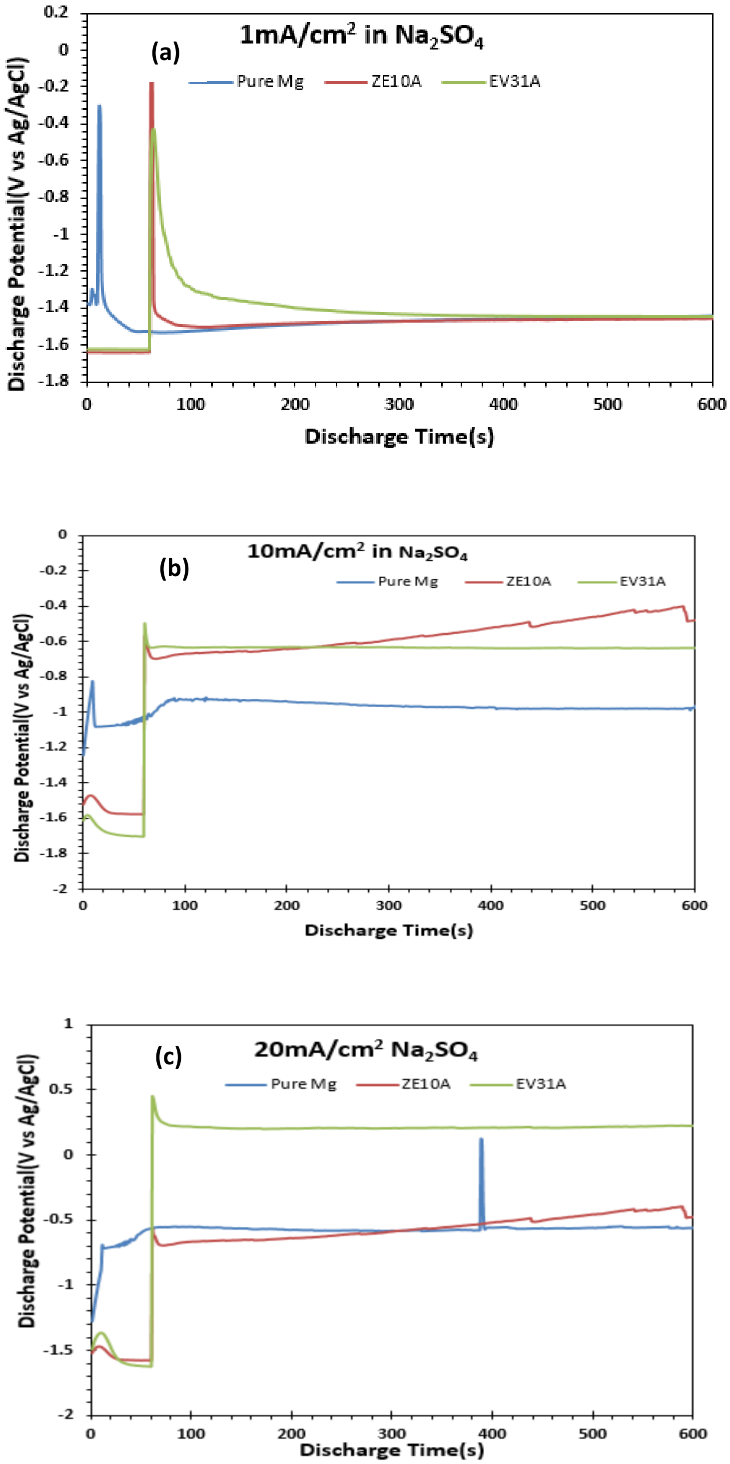

Figure 4.9 Discharge Behavior of Pure Mg, ZE10A and EV31A in 0.6M Na_2SO_4 at (a) 1ma/cm^2, (b) 10mA/cm^2 and (c) 20mA/cm^2

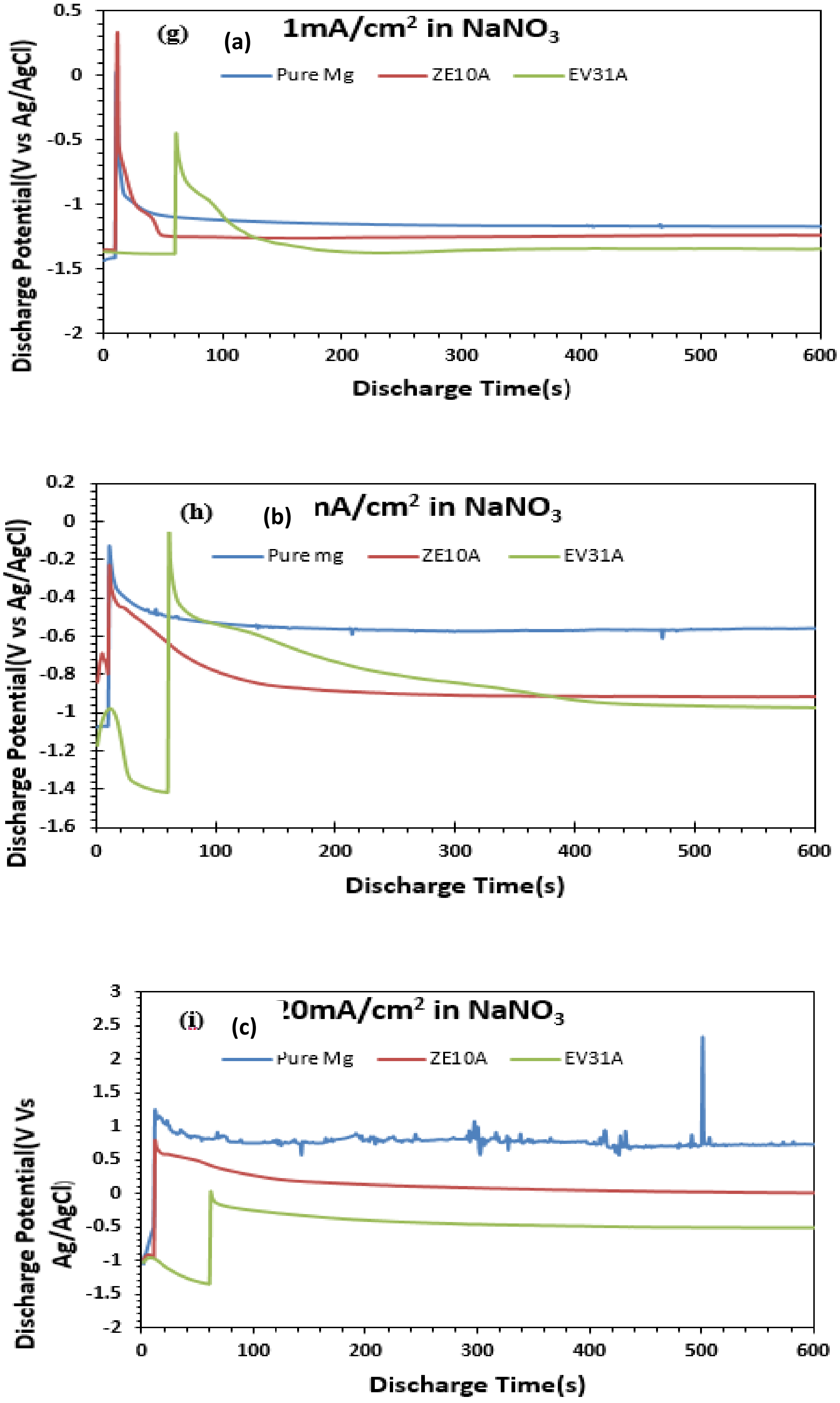

Figure 4.10 Discharge Behavior of Pure Mg, ZE10A and EV31A in 0.6M Na_2SO_4 at (a) 1ma/cm^2, (b) 10mA/cm^2 and (c) 20mA/cm^2

4.5 Analysis of Discharge Behavior of Battery

Figure 4.11 (a)-(c) shows the galvanostatic discharge behavior of Battery. EV31A showed the highest cell potential compared to ZE10A and Pure Mg at 1 mA/cm^2. The trend continues in case of 10mA/cm^2 , but pure Mg showed the highest cell potential at 20mA/cm^2. ZE10A showed discharge behavior between EV31A and Pure Mg in all three current densities. The cell potential for each battery had decreasing trend. The trend was smoother at 1mA/cm^2. The trend of cell voltage was rough in case of EV31A and ZE10A compared to Pure Magnesium at 10mA/cm^2 and 20mA/cm^2. This shows EV31A to be the better among the Battery anodes.

Figure 4.12 (a)-(c) showed the galvanostatic discharge behavior of battery after addition of arsenic oxide in the electrolyte. The cell voltage in case of ZE10A almost remained same with and without arsenic oxide. The cell voltage in case of EV31A and Pure Mg went down with the addition of arsenic oxide. The difference in the cell voltage was more with Pure Mg than EV31A.

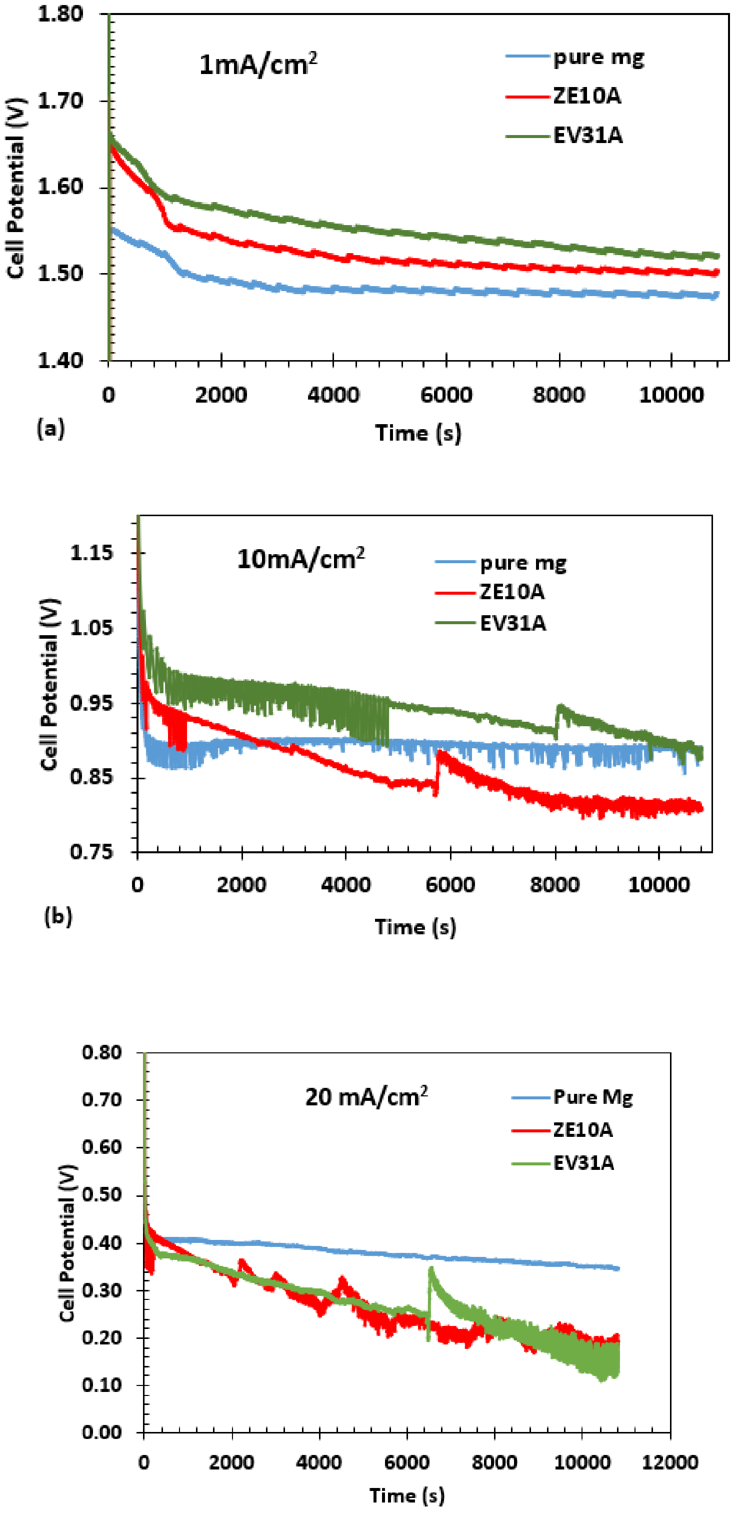

Figure 4.11 Discharge Behavior of Pure Mg, ZE10A and EV31A in battery at (a) 1ma/cm^2, (b) 10mA/cm^2 and (c) 20mA/cm^2

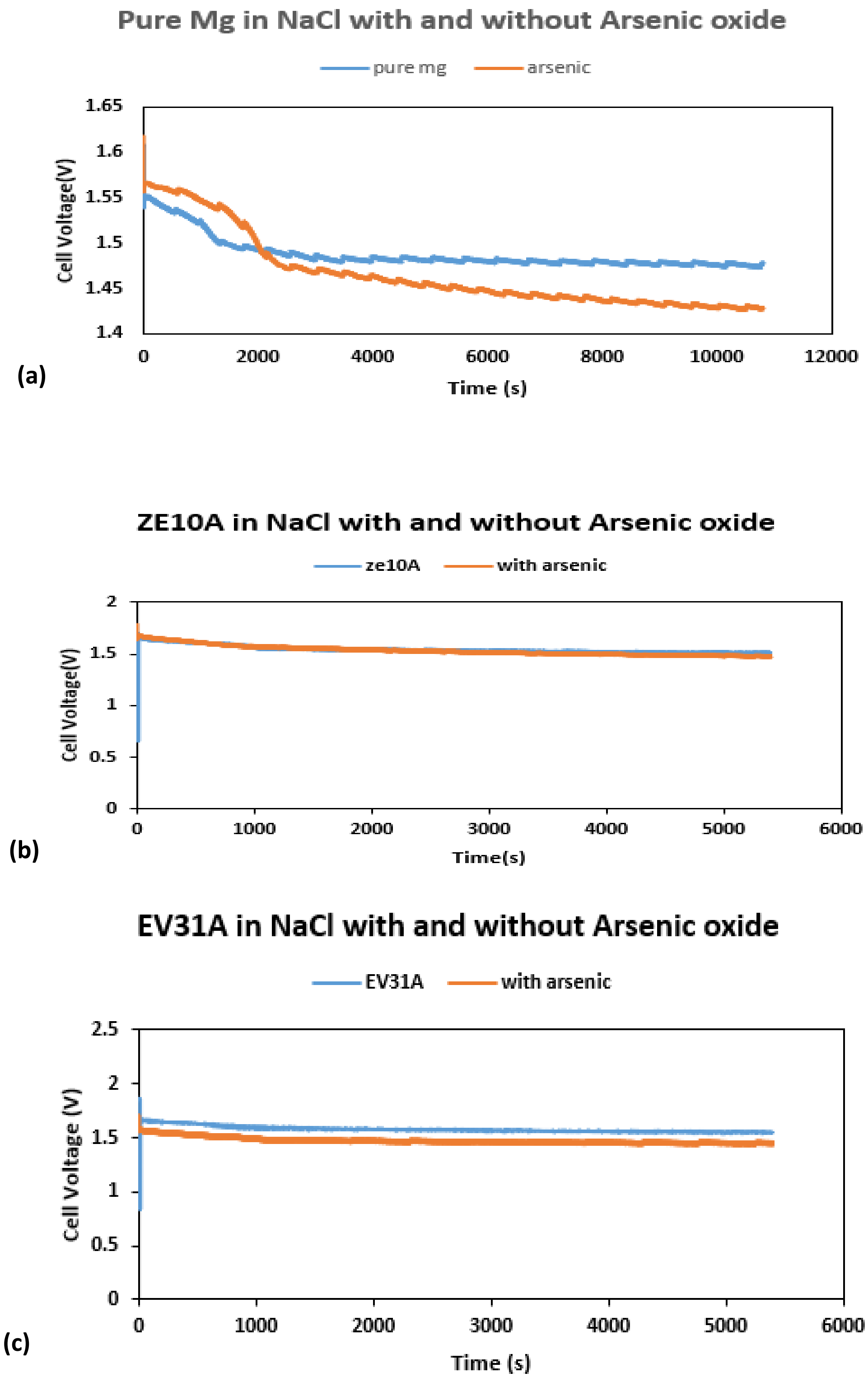

Figure 4.12 Discharge Behavior in battery with arsenic oxide of (a)Pure Mg, (b) ZE10A and (c)EV31A

4.6 Measurement of Efficiency

Efficiency of the anode material is calculated from the mass loss technique. The efficiency calculation given in the table 4.5 showed ZE10A to be the most efficient anode material. It showed the best faradaic efficiency at 1mA/cm^2 and 10mA/cm^2.

Table 4.5 Discharge Efficiency of Anode Materials Tested in the 0.6M NaCl Solution at Two Different Current Densities and MnO_2- Carbon Cathode Material

	Faradaic efficiency %	
Anode material	***1 mA/cm^2 for 3 h***	***10 mA/cm^2 for 3 h***
99.8% Mg	38 ± 4.6	34 ± 2.8
EV31A	48 ± 3.2	55.5 ± 1.6
ZE10A	68 ± 3.8	72.2 ± 2.3

4.7. SEM Analysis

The SEM pictures of sample were taken to observe the discharge products. The samples which were discharged at 10 mA and 100mA current density were observed under the SEM to observe the discharge properties of the samples in three different solutions. Figure 8 shows secondary electron images of the anodes surface after the discharge test at the current densities of 10 mA and100 mA for 600 seconds. It is observed that the discharge products are distributed over the whole anode surface in all three samples. The presence of crack was negligible in all three samples when dipped in $NaNO_3$ and constant and uniform layer of magnesium oxide layer was found on three samples which explains why hydrogen evolution and corrosion is very less in $NaNO_3$. The passivation is strong in $NaNO_3$ for three samples which prevents from further reaction and reduce hydrogen production. It is noteworthy that cracks could not be identified clearly in very low 10mA current density for pure magnesium. The cracks are starting to appear in EV31A and the cracks are already visible in case of ZE10A and EV31 A in NaCl. This explains the erratic discharge pattern in case of ZE10A in which irregular breakage of film cause SEM of ZE10A in NaCl in 10mA reveals the passivation layer slowly being decomposed and cracks appearing explaining the source of hydrogen evolution in the sample. It has been reported that the discharge properties of Mg batteries strongly depend on the morphologies of the oxidized surface. Different clumps of discharged products were observed in pure magnesium which are clumps of magnesium oxide films. The occurrence of cracks on the discharge products would also promote the penetration the solution electrolyte into the discharge products keeping in contact with the anode surface and retaining its discharge activity. The occurrence of cracks was more prominent in EV1A and ZE10A at 100mA current density. The figure 8 shows Mg in NaCl shows thick layer of magnesium oxide formation with shallow cracks at 10mA. The cracks were more visible at 100mA current density. This formation of thick discharge product with very few cracks on this surface prevents the electrolyte from meeting the anode surface resulting in the rapid voltage drop even at the low current densities. The activation mechanism of the magnesium alloy can be revealed by analyzing its discharge products which act as a barrier to the further oxidation of the anode material. It is obvious that the two products possess different morphologies. The discharge product of ZE10A displays more cracks than pure magnesium and EV31A shows more smooth cracking throughout the surface. The thick discharge products of pure magnesium present as large and dense micro blocks on the electrode surface reduces the electrode area leading to the weak discharge activity of pure magnesium when imposed a large current density.

The cracks are easily visible at 10mA/cm^2 and 100mA/cm^2 in case of ZE10A. The $Mg(OH)_2$ film is starting to break and the cracks formation is becoming more prominent at 10mA/cm^2 for ZE10A. This shows the difference in the rate of peeling off of the discharge product and the discharge layer which is causing the erratic discharge behavior of ZE10A. At 100mA/cm^2, the hydroxide layer seems to be almost completely broken down and cracks appear to be deeper. The formation of crack is uniform throughout the surface of ZE10A which cause a more stable discharge behavior in the alloy. The morphology of EV31A in NaCl is totally different from ZE10A as the surface is seen to be very uniform with a little crack initiation at the grain boundaries. This shows the need of higher potential to break the surface and thus causing the high discharge voltage compared to ZE10A at 10mA/cm^2. The crack growth seems to be more uniform than that of ZE10A which cause the stable potential compared to ZE10A at higher current density.

ZE10A seems to form a compact layer at 100mA/cm^2 in $NaNO_3$ compared to EV31 which has visible cracks compared to ZE10A. The visible cracks in EV31A shows a good discharge behavior by giving out more negative potential compared to ZE10A which has less activity due to formation of secondary precipitates in hydroxide film.

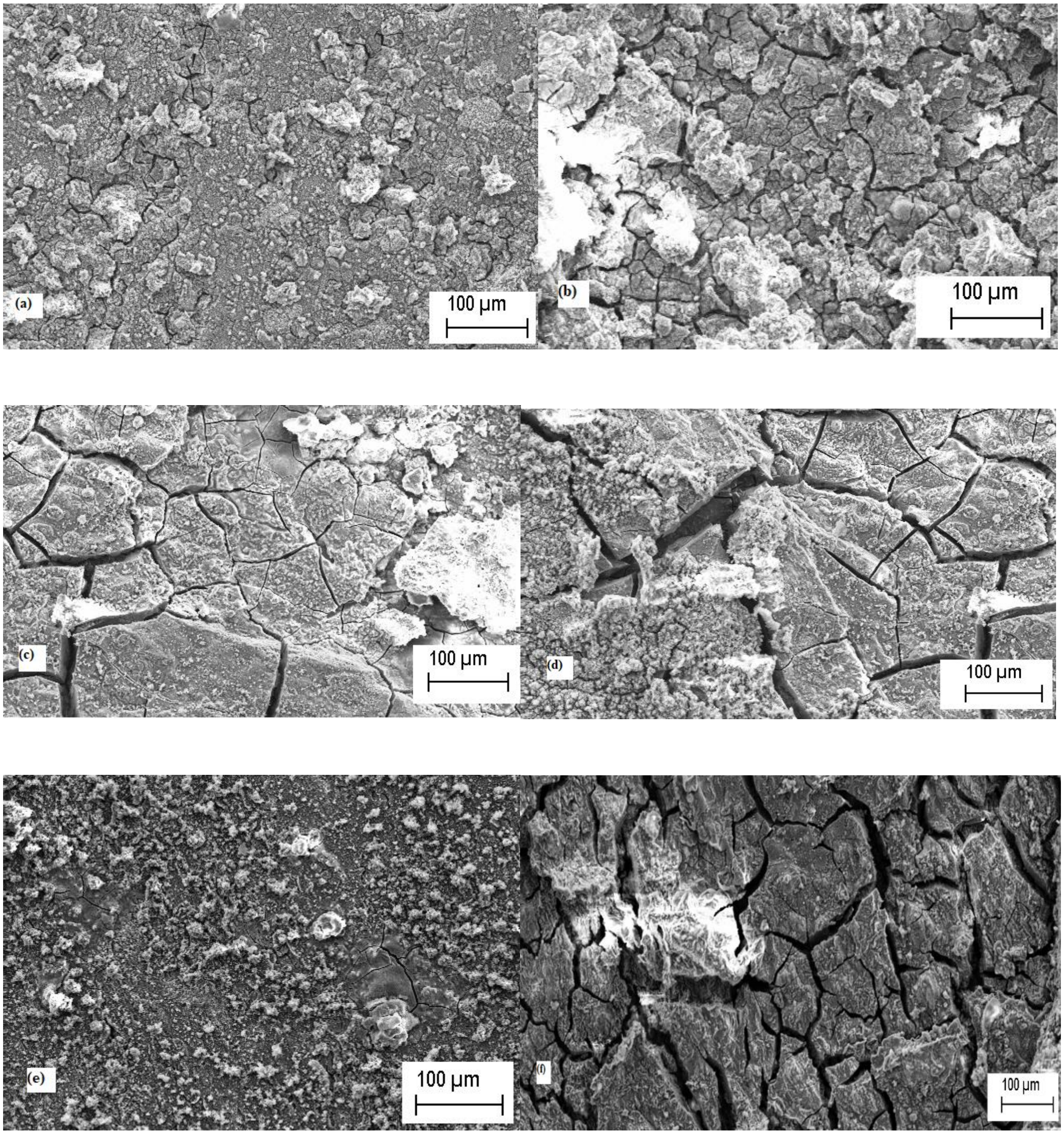
(a)
100 µm
(b)
100 µm
(c)
100 µm
(d)
100 µm
(e)
100 µm
(f)
100 µm

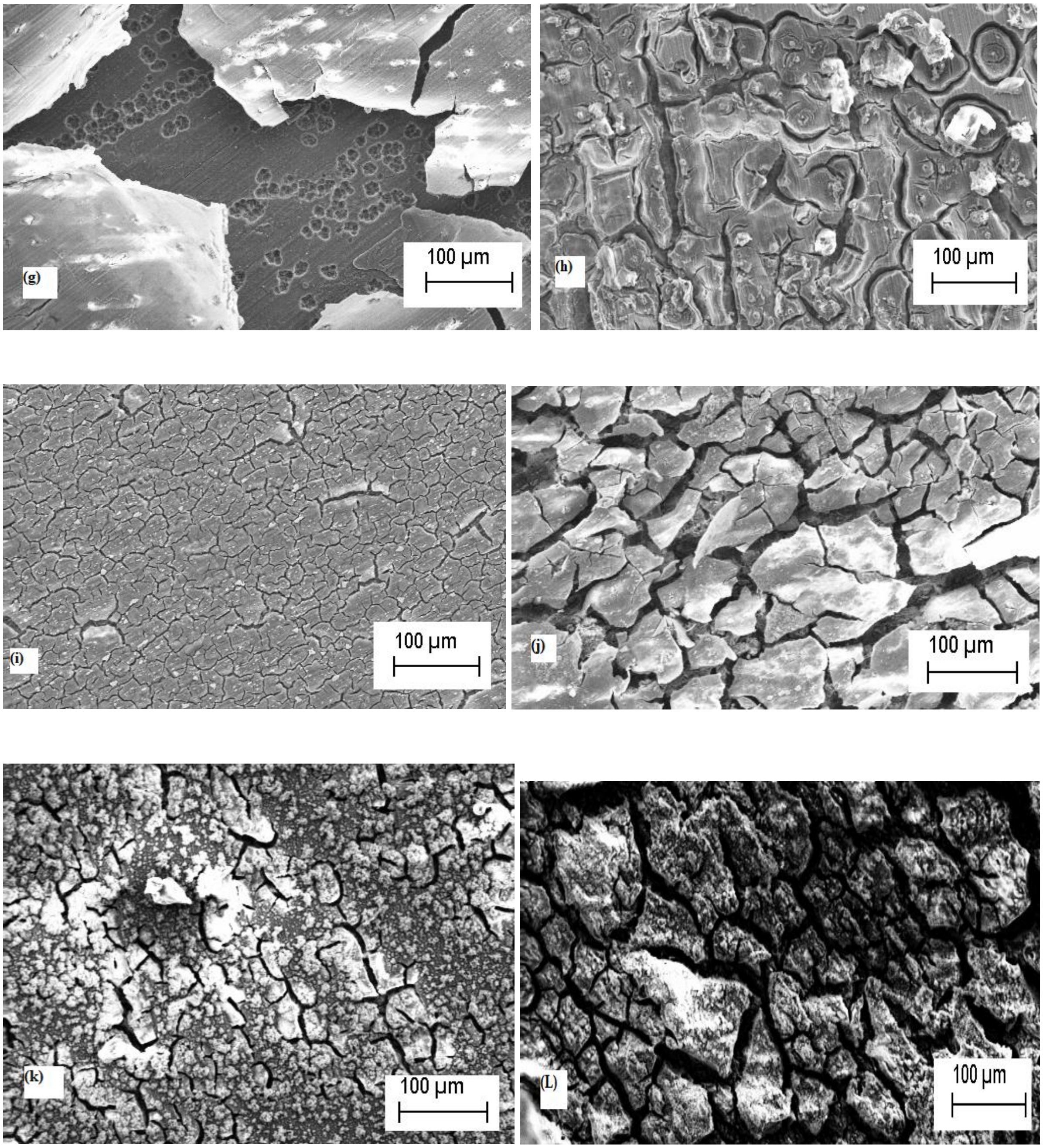
(g)
100 µm
(h)
100 µm
(i)
100 µm
(j)
100 µm
(k)
100 µm
(L)
100 µm

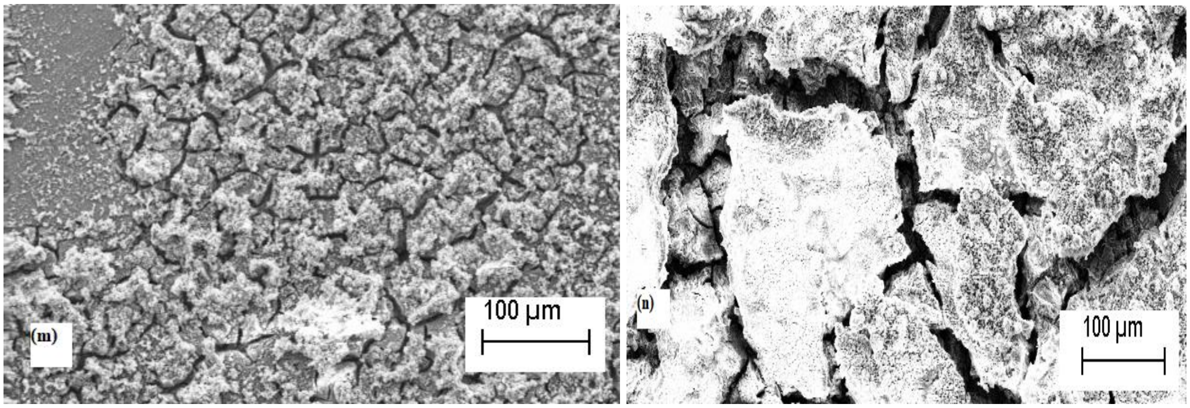

Figure 4.13 SEM micrograph of three samples discharged at 10mA/cm^2 and 100mA/cm^{2}current densities in three solutions: (a)-(b)Pure Mg in NaCl , (c)-(d)ZE10A in NaCl,(e)-(f)EV31A in NaCl, (g)-(h) ZE10A in $NaNO_3$,(i)-(j) EV31A in $NaNO_3$, (k)-(L)ZE10A in Na_2SO_4 and (m)-(n) EV31A in Na_2SO_4.

Chapter 5 Conclusion

- EV31A showed the most active corrosion potential among the alloys but was comparatively polarizable. It had higher corrosion rate than Pure Mg and ZE10A
- EV31A had the highest overpotential than Pure Mg and ZE10A which means hydrogen is evolved comparatively lesser than the two alloys. Hydrogen generation rate was comparatively lower in Mg-RE alloys than Pure Mg two RE alloys.
- Pure Mg had the highest impedance which made it more resistant among the three before discharge. But after discharge, EV31A showed higher impedance except in $NaNO_3$ in which Pure Mg had the most resistance.
- The galvanostatic discharge showed EV31A to give out the highest cell voltage among the three electrodes. The cell voltage of EV31A was better than ZE10A and Pure Mg except at $20mA/cm^2$ which means the battery is useful for lower power applications.
- ZE10A showed the best efficiency among the materials followed closely by EV31A as potential anodes for battery material.
- Addition of Arsenic oxide in 0.6M NaCl showed the lower cell voltage as well as low hydrogen evolution reaction.